TECHNICAL REVIEW

No.21 / March 2024

Technical Review
MAPNA TURBINE ENGINEERING & MANUFACTURING CO. (TUGA)

TUGA
MAPNA GROUP

Willpower to Empower Generations

Cover Page:
MAPNA Turbine's Axial Compressor Test Stand

Editorial

Dear Colleagues, Partners and Professionals,

Here at MAPNA Turbine, we constantly endeavor to extend our influence in the market and create value for our customers by further developing our products and methods, as well as portfolio of services. It is in this context and with great pleasure that a brief account of a few recent technological achievements is presented to you, our valued readers, in this edition of MAPNA Turbine Technical Review.

Acknowledging the importance of exploring new methods and techniques to achieve further enhanced and more effective axial compressor designs, MAPNA Turbine has set up its axial compressor test stand and is constantly testing cutting-edge ideas in this field. The first article highlights the most important steps taken to design and manufacture this test stand on premises.

As an investigation into Urmia CCPP case study in which an unanticipated temperature rise in thrust bearings of an MGT-70 unit was observed, the second article delineates the efforts made to identify and analyze spark erosion as the root cause of this incident, along with the measures taken to address this issue.

The third article reviews the aerodynamic and mechanical design process of MAPNA Turbine's brand new, high-pressure centrifugal compressors which are specifically used for injecting gas into underground reservoirs in hot seasons to save it for later use in cold seasons when gas demand grows.

Details of an innovative CFD approach used to attain turbocharger compressor performance map are outlined in the fourth article. This approach brings about significant reduction in calculation time and has proven to be a reasonably accurate one in the development of this product.
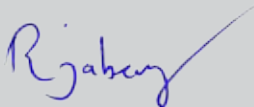
The last article takes an in-depth look into Vacuum Brazing method, carried out in MAPNA Turbine for impeller production. Different fillers were evaluated and further tests were conducted on samples brazed with gold-based filler (identified to result in stronger joints) to ensure that the design requirements are met.

Please join us in relishing a detailed account of these subjects in this issue of the Technical Review.

Respectfully,

Roohollah Jabery,

Vice President of Engineering and R&D

MAPNA Turbine Company (TUGA)

March 2024

Contents

Introduction

Performance characteristics of axial flow compressors hold great importance to design engineers when it comes to stable and desirable operation of gas turbine engines. To achieve enhanced performance characteristics, modern axial flow compressors take advantage of cutting-edge blade designs, which were rarely achievable using traditional methods. On the other hand, achieving the intended results out of the advanced blade technologies and new design tools requires appropriate hardware capable of performing experimental tests and verifications. Recognizing the importance of these evaluations from both aerodynamic and mechanical perspectives, MAPNA Turbine decided to set up an axial compressor test stand aiming to enhance the reliability and effectiveness of axial compressor development process.

Specific details of this compressor test stand design were elaborated on in Technical Review No. 9. In the design process, special attention was given to utilization of the available centrifugal process compressor test bench facilities and several key parameters from that test bench, such as electrical motor, air piping, test bed geometry, cooling and lubrication system, as well as PLC-based control system were benchmarked. Below is a brief description of design characteristics and compressor performance parameters of the test bed, followed by manufacturing remarks, control system details and commissioning program. This report ends with presenting some test results and plans for the future activities.

1

Axial compressor test stand: From Concept to In-house Test Facility

Pakatchian, Mohammad
Ranjbaran, Alireza
Faghfoor, Saeed

MAPNA Turbine Engineering & Manufacturing Co. (TUGA)

Compressor Test Stand Design Characteristics

The design process of axial flow compressor follows a systematic and step-by-step approach, which involves continuous collaboration and iterative exchanges between the aerodynamic design based on input data, and mechanical design to handle structural aspects. This back-and-forth process ensures that the aerodynamic and mechanical considerations are effectively integrated into the final design. The obtained axial compressor comprises five stages. The first stage contains 3D-designed transonic blades to augment compressor mass flow and efficiency. A 3D section view of the compressor is illustrated in Figure 1 and the key parameters are summarized in Table 1.

Table 1- Compressor design parameters

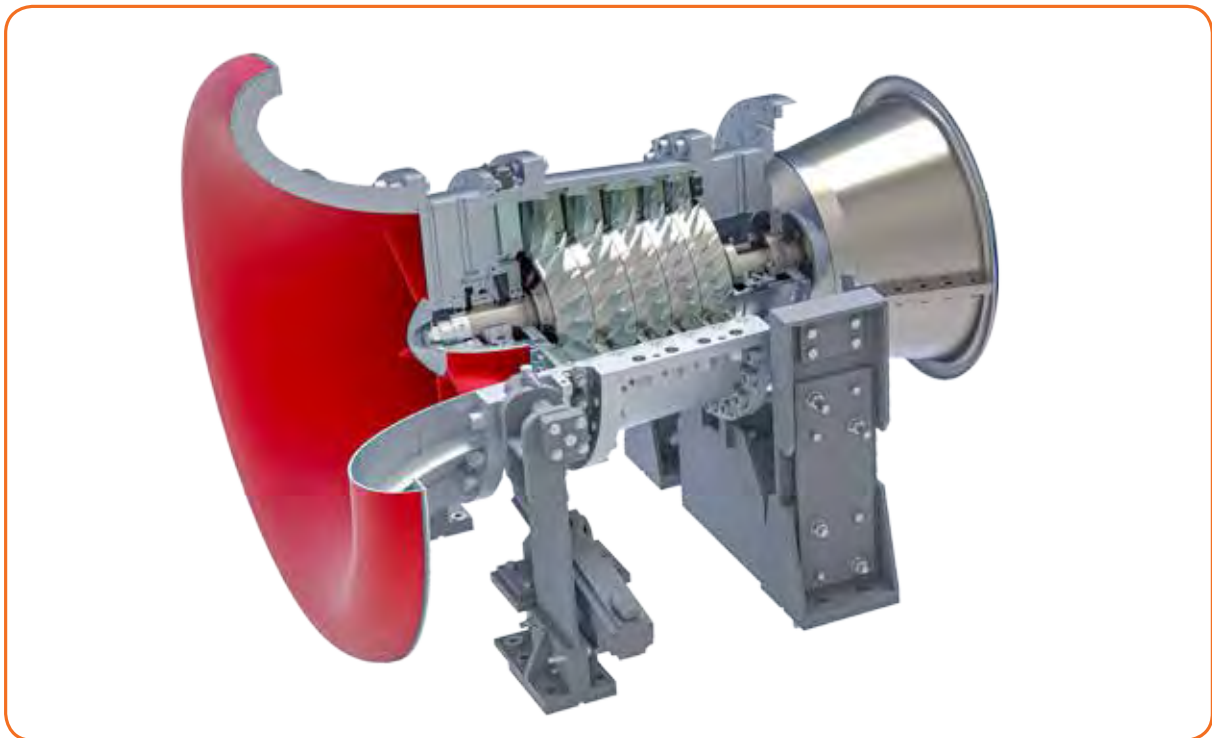| Parameter	Value
Mass flow rate	19 kg/s
Number of stages	5
Pressure ratio	3.2
Isentropic efficiency	89.1 %
Rotational speed	15700 rpm

Figure 1- Compressor section view

Considering the adaptability to various operating conditions, a specialized Inlet Guide Vane (IGV) mechanism was designed and integrated into the compressor. The inclusion of the IGV provides a broader range of experimental evaluation and enhances flexibility in fine-tuning and optimizing the system performance to meet specific demands of different operational conditions. The schematic P&ID of the compressor test stand including the main parts is depicted in Figure 2, while the assembly model of the compressor, gearbox, inlet plenum, exhaust adaptor and required substructures are shown in Figure 3.
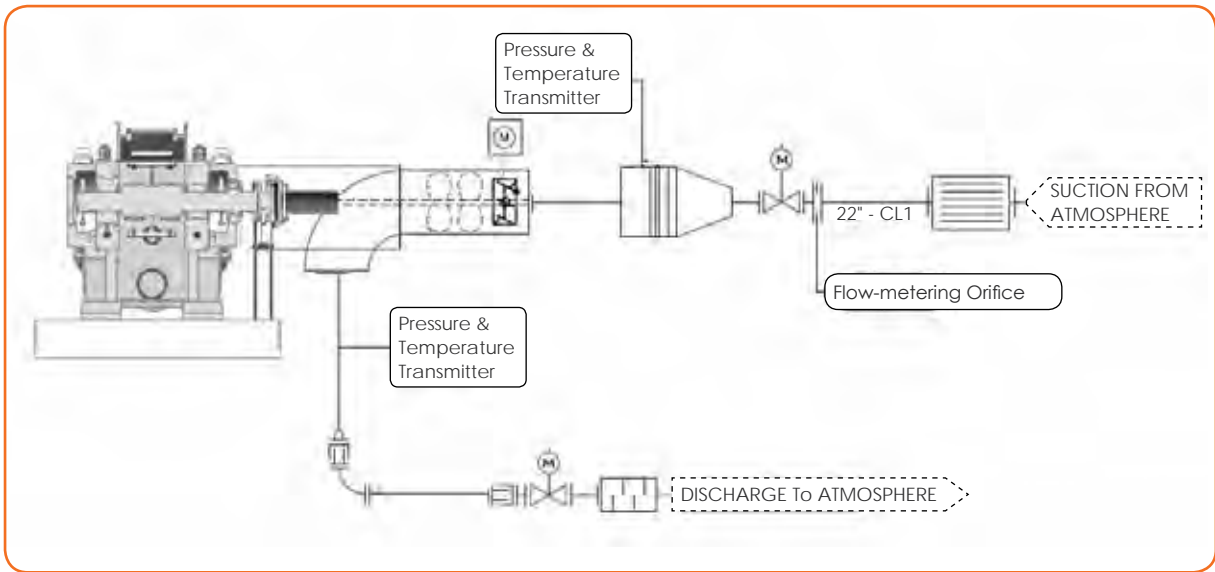
Figure 2- P&ID

Figure 3- On-skid compressor model

During the design phase, evaluation of the performance and stability of the compressor was achieved by developing characteristic maps, which were generated through numerical simulations conducted at different rotational speeds, compressor exit pressure settings, and various positions of the inlet guide vanes (IGV). Figure 4 and Figure 5 illustrate the normalized performance characteristics of the compressor with IGV set in open and close positions respectively.
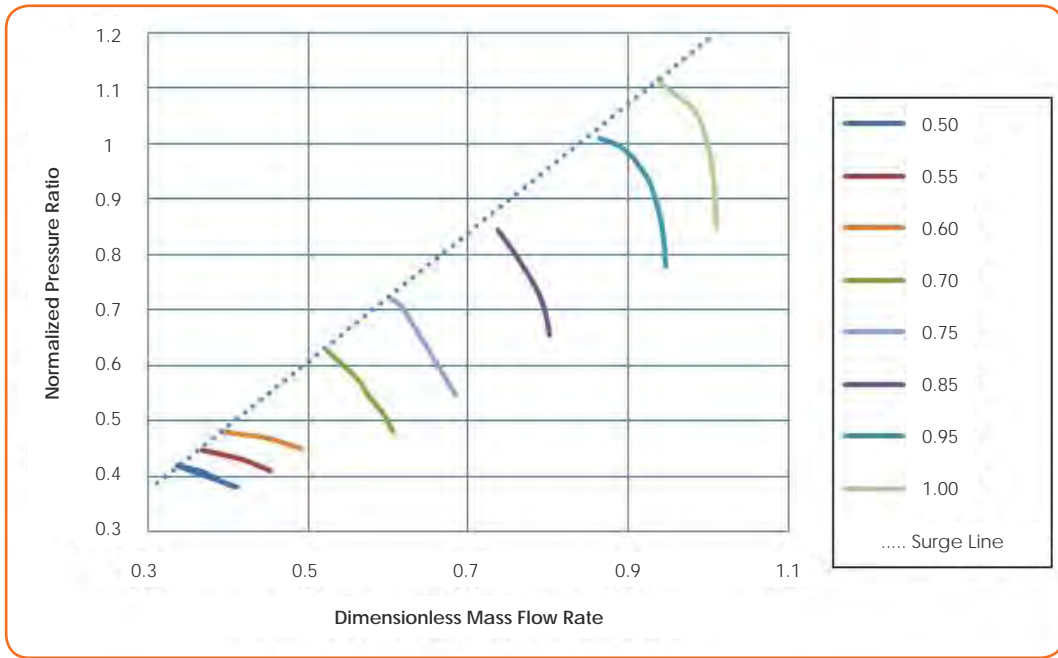
Figure 4- Compressor characteristics at open IGV position
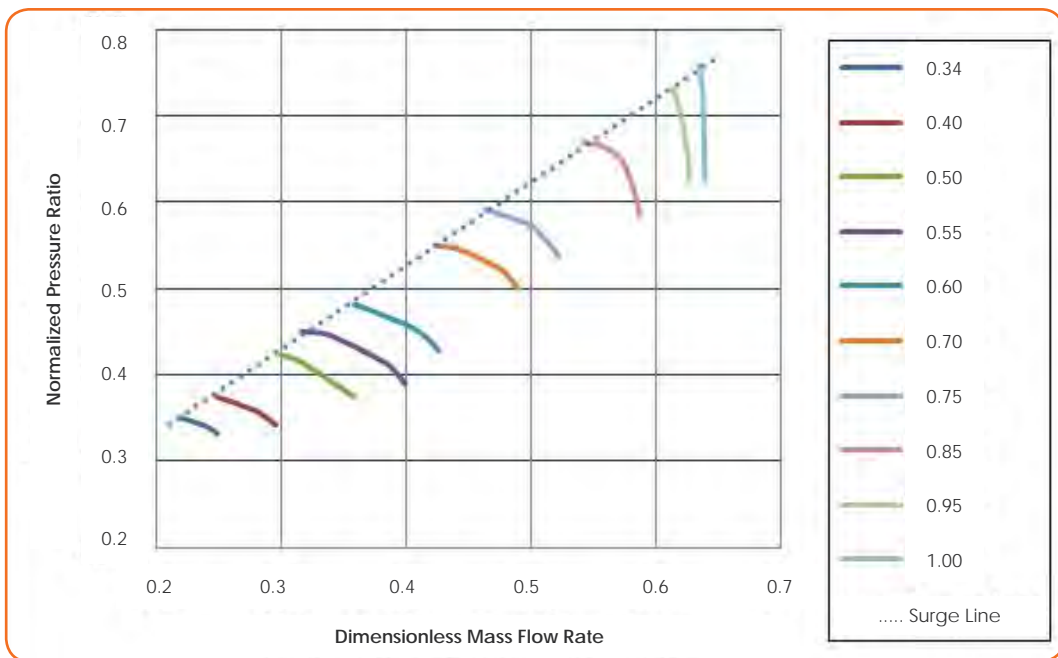
Figure 5- Compressor characteristic at closed IGV position

Manufacturing and Assembly Highlights

As mentioned, mechanical design features of the compressor test stand were outlined in Technical Review No. 9, with the exception that rolling bearings are now replaced with hydrodynamic bearings and the rotor dynamic analysis was as a result updated accordingly. The cross section of the core compressor is illustrated in Figure 6.

Figure 6- The cross section of a 5-stage axial flow compressor

The compressor blades (stationary, rotary and IGVs) are made of stainless steel, machined using 5-axis CNC machines within the TUGA Company. Shafts, rotor discs, as well as central tie-rod and nut which 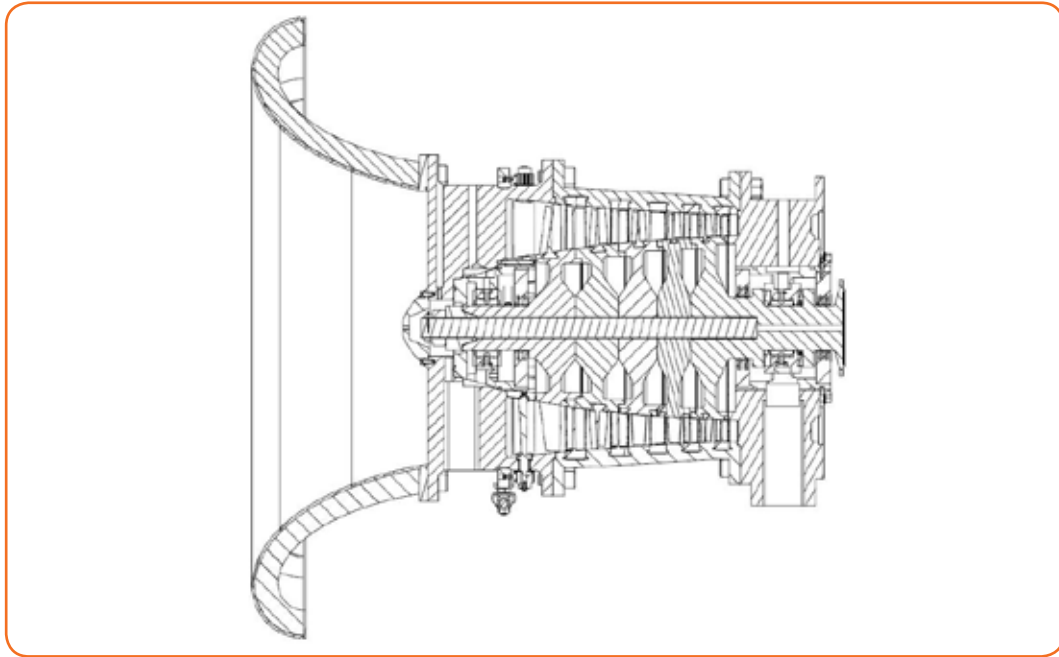play important roles in the integration of the compressor rotor, are manufactured through advanced machining from high-quality alloy steels, chosen specifically for their exceptional strength and durability to withstand the demanding operating conditions. The compressor casings, consisting of the inlet, intermediate, and outlet casings are manufactured from cast steel regarding their geometry and design features, such as the presence of struts. During the subsequent machining stage, required features of the casings such as stationary blade slots, struts, junctions, as well as holes required for instrumentation and bearing lube oil tubing are established. It is worth noting that the intermediate casing comprises two separate halves, namely the lower and upper parts, while the inlet and outlet casings are integrated as a single unit due to manufacturing and assembly considerations. The special design of intermediate casing allows for easier access for maintenance and repair with minimal required intrusion and disassembly of other parts.

The IGV actuation mechanism is comprised of a rack, pinions, and related joints. The rack plays a crucial role in adjusting the angle of the IGV blades, allowing for precise control of the airflow. The pinion, serves as the driving mechanism for the IGV system. It engages with the rack, translating rotational motion into the desired blade angle adjustment. Design and manufacturing of the pinion were carefully executed to ensure reliable and accurate operation. In addition to the rack and pinion, various related joints are incorporated into the IGV mechanism. These joints provide necessary linkage and articulation points to ensure coordinated movement of the IGV components. Their precise fabrication and assembly are crucial to maintaining the integrity and functionality of the mechanism.

The assembly process follows a specific sequence, ensuring the integration of the components in an efficient manner. Initially, the stator assembly is completed, addressing any discrepancies, and ensuring proper alignment. Simultaneously, the rotor assembly is also accomplished, encompassing the necessary components and ensuring their integration. Once both the stator and rotor assemblies are prepared, they are brought together in a predetermined order.

Due to the high rotational speed of this equipment and concerns about vibration issues, three balancing sequences are applied including balancing of individual discs, balancing of bladed discs assembly, and complete rotor balancing. By performing these actions, a satisfactory level of balance is achieved.

Figure 7- Bladed disc balance procedure

Instrumentation and Control System

The axial flow compressor test stand is designed to be operated in safe conditions by applying required controls and protections. To ensure the normal operation of the compressor, a comprehensive array of sensors and instruments are incorporated into the test stand. The most important aspect of protection is the inclusion of vibration sensors, which are strategically located on the compressor and bearing casings with the corresponding actions defined in the PLC-based control system logic. The oil temperature measurement is also critical for ensuring the safe operation of bearings and the required RTDs are installed on the inlet and outlet pipes in addition to the bearing pad temperature monitoring instruments.

Measuring air pressure and temperature at the plenum and discharged line is crucial for assessing the flow characteristics of the compressor and maintaining its stability. These measurements and their accuracy play a key role in preventing compressor surge, a condition that can disrupt the compressor's performance and efficiency. In fact, the surge margins (pressure ratio limit) at any operational condition have been calculated based on the obtained compressor map and flow parameters. To accurately measure the inlet flow rate, an orifice-type flow meter is installed at the upstream of the plenum. This flow meter is specifically designed based on ISO 5167 standards, ensuring precise and reliable flow rate measurements. The data obtained from the flow meter enables the control system to accurately evaluate the compressor's performance and efficiency.

By incorporating these monitoring and control features, the axial flow compressor test stand provides a reliable and safe environment for testing and evaluating the performance of compressors. The data collected from these sensors and instruments facilitate precise analysis, optimization, and performance enhancement of compressors under various operating scenarios. It is also planned to implement an advanced data gathering system in the future,

specifically to extract precise information about the properties of the airflow passing through the compressor stages. Implementation of this system needs additional modifications to the compressor casing, including the incorporation of rakes and probes within the internal flow path. Moreover, procedures are carried out on the stationary blades to facilitate the installation of pressure tapping on both the suction side and pressure side of the blades. These measures are intended to optimize the measurement and analysis of airflow within the compressor, ensuring even greater accuracy and reliability.

Test Stand Commissioning

The compressor test stand commissioning procedure is initiated with emphasis on ensuring the stable operation of the entire system. To achieve this, additional protective measures and sequences are implemented regarding both gear box commissioning instruction and compressor operational limitations especially on safe rotational speed margins. The evaluation of the compressor's safe operation begins with examining its performance under pre-defined low to medium rotational speeds and the tests are conducted firstly at minimum load by closing the IGV and opening the discharge line valve. Following that, by running the compressor at different rotational speeds and changing the position of IGV and discharge valve, the operating range in which the compressor could safely operate is determined. In fact, the evaluation of the compressor's design is carried out according to a systematic step-by-step procedure. Each step is carefully executed to ensure that the pressure ratio controller setpoint is aligned precisely with the predetermined design specifications. Additionally, the reliability and practicality of control system are checked and necessary modifications are performed on its programming, logic and settings.

The HMI displayed in Figure 8 functions as a centralized interface for gathering essential data on various parameters such as pressure, temperature, mass flow, lubricant temperature, and vibration data. By consolidating these critical parameters into a single page, the HMI facilitates easy access to information, and real-time data analysis, fostering efficient decision-making and ensuring optimal functioning of the system. This comprehensive data gathering system not only provides research engineers with an integrated overview of the system's operation, but also empowers operators and maintenance personnel to closely monitor key parameters and make adjustments when necessary.
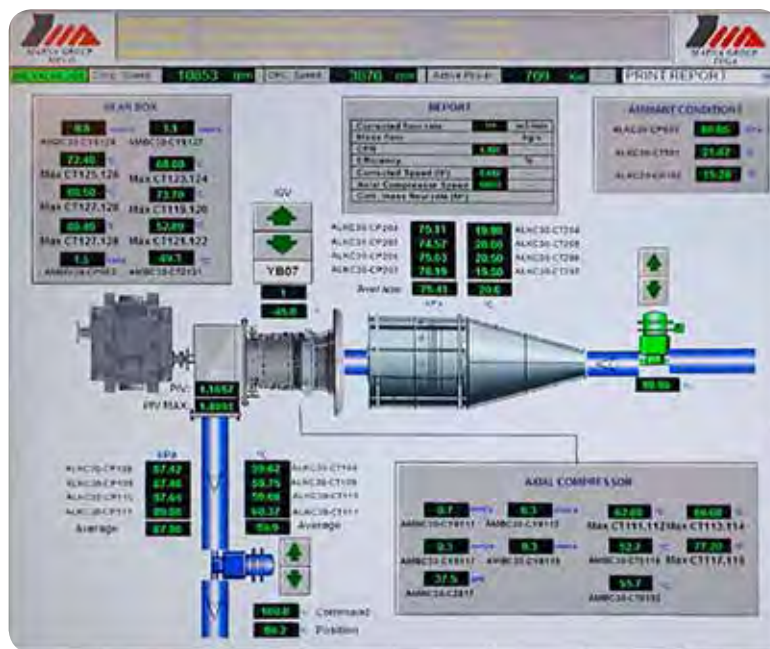

Figure 8- Axial compressor test-stand's main HMI

Figure 9 illustrates the sequential method for gradually raising the rotational speed of the compressor while staying within specific mechanical boundaries. The procedure commences with the IGV in a closed position and the discharge valve fully open, facilitating unobstructed airflow discharge. This preliminary step plays a crucial role in assessing vibration limits and shaft displacements before imposing any extra load on the compressor blades.

As the process progresses, the IGV gradually opens, adjusting the closed positions of the discharge valve to regulate the throttling of the compressed air and increasing discharged pressure respectively.
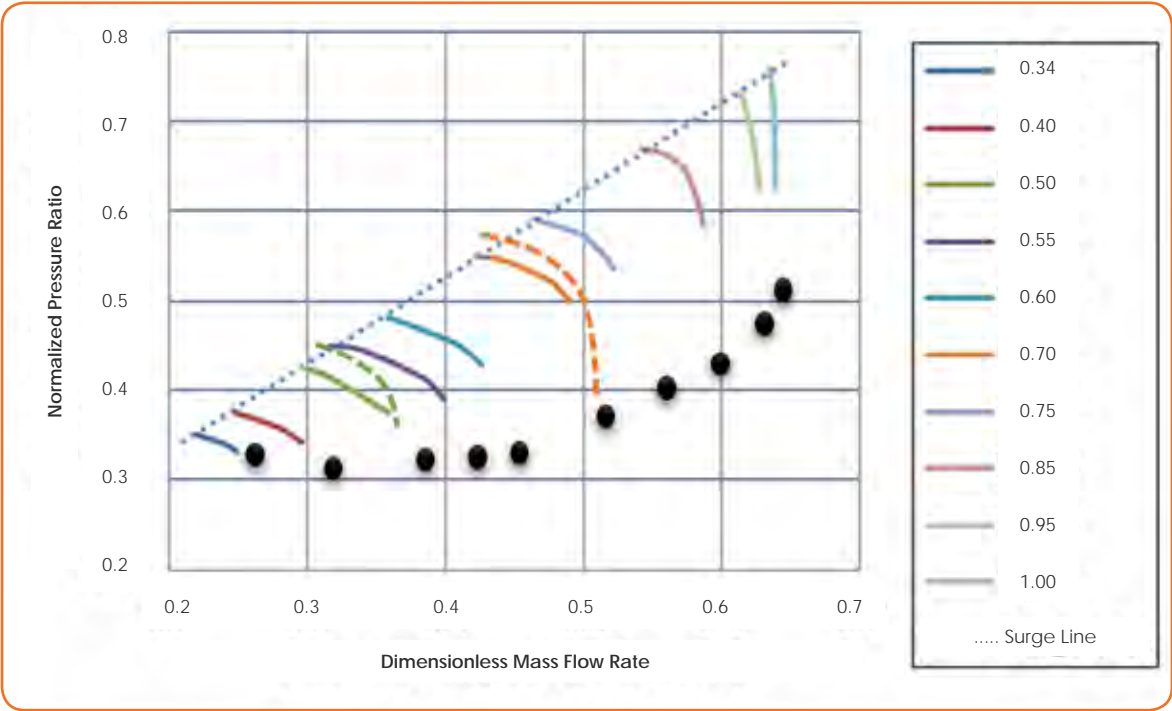

Figure 9- Test data for closed IGV and minimum pressure ratio

Concluding Remarks

The recently constructed axial compressor test stand has been tailored to meet the needs of advanced technologies as well as enable test and validation of compressor designs based on conventional blade technology. Its primary purpose is to facilitate the testing and evaluation of newly developed techniques deployed to upgrade existing products, or develop innovative technologies related to the design of high efficiency gas turbine compressors. These technologies may contain various crucial aspects, including the evaluation of highly loaded blades, Variable Guide Vane (VGV) mechanisms and system integrity with inlet and outlet air system. This test stand also gives the engineers the chance of investigating innovative methods to improve compressor performance, such as end wall treatments and the effects of micro grooves on the blades beneath the boundary layer. Additionally, the test bed offers the opportunity to examine the feasibility and effectiveness of new ideas by integrating machine learning techniques and design optimization. This enables a comprehensive understanding of the potential benefits and effectiveness of these approaches. Moreover, development of this facility fosters collaboration with academic institutions, providing a platform for knowledge sharing and the development of novel concepts.

2

The Significance of Electrical Pitting in Temperature Rise in Hydrodynamic Thrust Bearings

Introduction

Turbine hydrodynamic bearings are basically designed with sufficient margin to handle normal operating conditions. However, there is a potential threat called spark erosion that can cause significant damage to these bearings. Spark erosion occurs when electrical discharges from the generator pass through small gaps in the bearing, gradually eroding babbitt surface and resulting in bearing dysfunction.

In this article, details of a case study in which spark erosion led to unanticipated temperature rise in thrust bearing of an MGT-70 unit shall be outlined; and efforts made to identify and analyze the root cause of this incident will be explained.

Jenabi, Farhad
Shojaeyan, Alireza

MAPNA Turbine Engineering & Manufacturing Co. (TUGA)

Case Study: Urmia Combined Cycle Power Plant

In MAPNA Turbine fleet, spark erosion was first detected in gas turbine unit 3 of Urmia CCPP. After upgrading the turbine to version T90, its thrust temperatures started to gradually rise to 100°C during operation at elevated loads, till its main thrust bearing temperature suddenly exceeded the trip limit of 120°C. Although it was discovered that the babbitted layer on all main thrust pads had been wiped out, the underlying cause remained unidentified at that time. After replacing the pads, the main thrust temperatures continued to rise, necessitating power limitations to inhibit them. Whenever the unit was approaching the base load, temperature of the thrust pads on main side showed constant increase with an unrecoverable drift. Even with limiting the power to decrease the thrust temperatures, the phenomenon resurfaced as soon as the load increased again.

Temperature Trends in Main Thrust Bearing

Monitoring the operating parameters in two time periods after emergency repairs (Figure 1) showed that the maximum daily temperatures of the main thrust bearing had upward trends despite several corrective actions taken, including bearing or thrust pads replacement, turbine oil refilling, and modifying orifice diameters in lifting oil lines.

After inspecting the pads during second emergency repairs, electrical discharge was identified as the root cause of the bearing failure. Following a modification to generator grounding system in order to prevent the electrical discharging through bearing, the rising temperature was controlled.
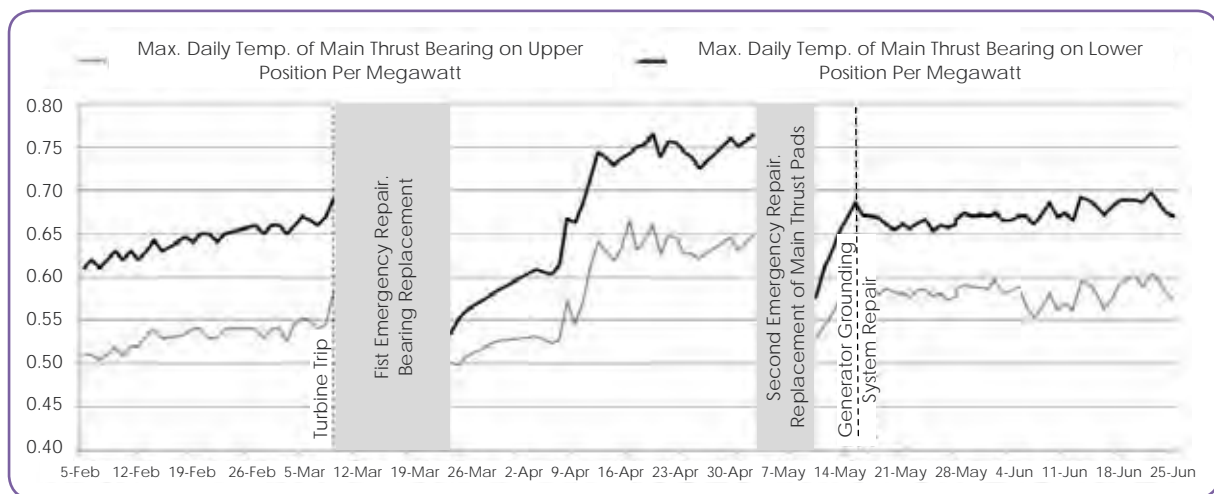

Figure 1- Trends of maximum recorded daily temperatures of main thrust bearing on upper and lower positions per megawatt

Inspecting Bearing Thrust Pads

On the babbitt surface of each thrust pad, a rough region was detected extending from the trailing edge towards the middle area, as shown in Figure 2. This effect, referred to as spark erosion or electrical pitting, consists of material removal from the pad surface as a result of electrical discharge.

Figure 2- Pattern of damaged areas on babbitt surface of main thrust pads in gas turbine Urmia-3 detected during the second emergency repair

Using a microscope revealed crater-shaped depressions and roughly hemispherical pits. Figure 3 shows a closer view of the pitted marks where there is a clear boundary between pitted and unpitted regions. Furthermore, measurements indicated a decrease of 0.1 mm in babbitt thickness within the pitted region, resulting in reduction of load carrying thrust area of each pad.
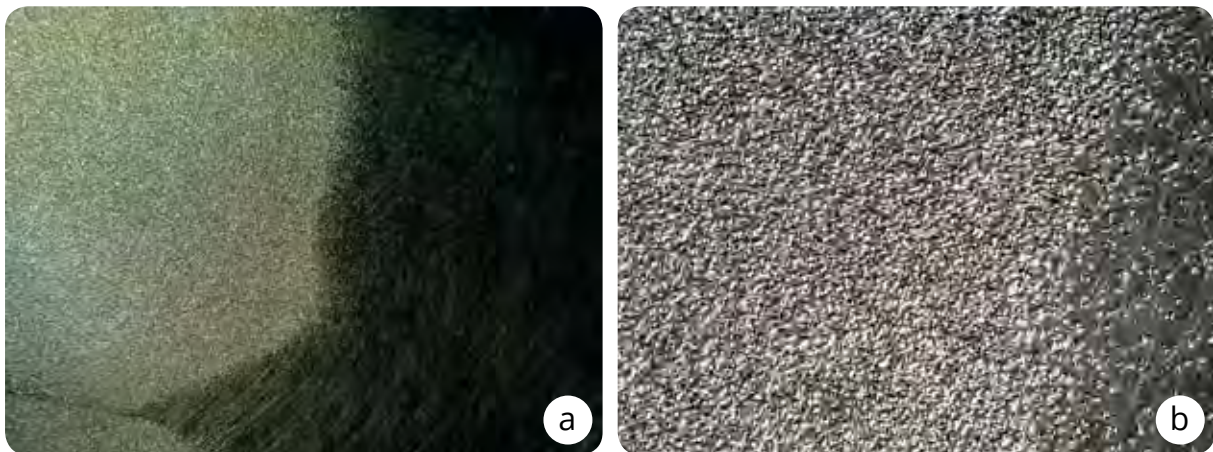

Figure 3- Electrical pitting damages on babbitt surface of main thrust pads in gas turbine Urmia-3 with (a) 6 times and (b) 40 times magnification

Electrical Pitting as the Root Cause

Electrical pitting occurs in hydrodynamic bearings by intermittent arcing of electrical current due to voltage discharge when the oil film is extremely thin. The electrical current follows the path with the least resistance, which is near the trailing edge of the thrust pads on the main side in this bearing (Figure 4). This position does not necessarily coincide with the minimum oil film thickness since the resistance of the oil depends on various factors; however, it tends to be close to the trailing edge of the thrust pads. As output power is increased to the base load, oil film thickness is expected to decrease in order to balance the axial load. As a result, the babbitt material of thrust pads gets damaged by the electrical discharges, leading to reduction of load carrying capacity. Consequently, the oil film thickness would further decrease to tolerate the axial load, causing a change in tilting angle of the pads and an increase in the thrust bearing temperature. The aforementioned damages gradually propagate towards the leading edge of the pads; eventually the oil film can no longer withstand the load, and all the pitting marks will

be wiped out. As the bearing continues to take the load, the oil film recovers on the thrust pads and electrical discharges reoccur at the trailing edges. This cyclical process might repeat several times until insufficient amount of babbitt material remains in place which would eventually lead to bearing failure [1].
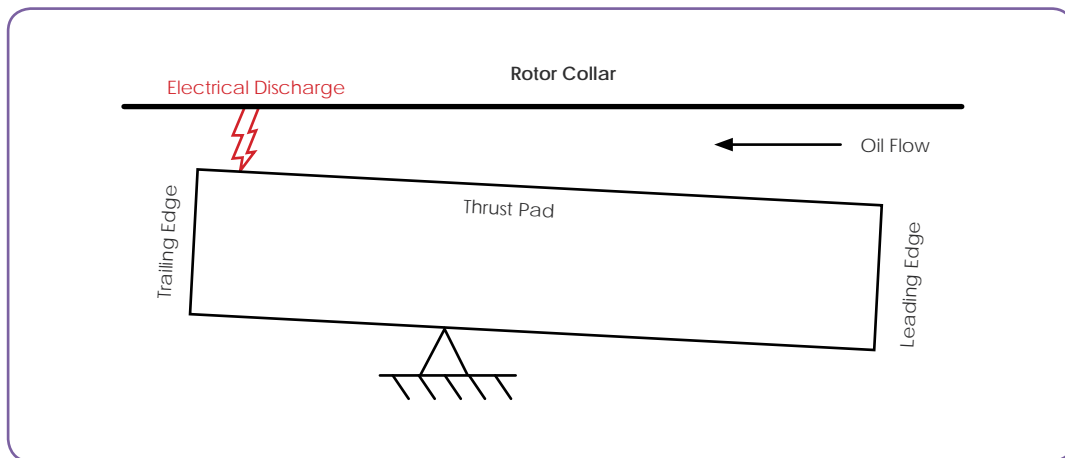

Figure 4- Schematic illustration of a thrust pad during bearing operation considering potential of electrical discharges from the rotor

Damages to the bearing can occur at potentials even below one volt. The consequences of arcing include the removal of metal fused in the arc, followed by accelerated mechanical wear. When an electrical discharge takes place between the thrust pads and the collar face of a rotor, it generates localized heat that causes the babbitt metal to fuse, resulting in debris that contaminates lubricating oil [2]. The magnitude of temperature rise in a hydrodynamic bearing depends on several factors, including axial load on the bearing, severity and frequency of the electrical discharges, design of the bearing, and lubrication conditions.

Stray Currents in Generators

Electric currents that flow unintentionally in generators can be caused by both electrostatic and electromagnetic fields. Electromagnetic shaft currents are stronger and more severe than electrostatic currents. When a current passes through generator windings, it generates a magnetic field that can interact with nearby conductive structures, leading to the induction of stray currents. The magnitude of magnetic field required to excite the shaft currents decreases as the size of machine and its rotation speed increase. The strength of stray voltages or currents depends upon the strength of residual magnetic fields, clearances between rotor and stator components, available paths for the currents, insulating properties of oil film in the bearing, and other relevant factors [3]. To prevent electrical discharge through the bearing, it is recommended to utilize carbon brushes or copper straps between rotor and stator of the generator. Additionally, electrical insulation might be added to the bearing structure. The induced voltages on the shaft must be recorded from the very first start of the generator and it is recommended to measure it periodically during operation [4]. Increasing shaft voltages over time indicates poor contacts between the shaft and its grounding system, and it is essential to ensure the effectiveness of all grounding connections.

Figure 5- Contact of flexible copper braids with rotor of a generator for discharging stray currents

Since grounding system had not been checked during overhaul of generator unit 3 at Urmia CCPP, whenever the power was elevated, shaft currents would discharge through the thrust pads due to reduced gaps in the bearing. After adjusting or replacing the grounding brushes/braids, shaft voltages were measured using an oscilloscope indicating that the electrical discharges through the bearing were halted. Furthermore, by monitoring the operating parameters of the unit, it was assured that the thrust bearing temperature was well controlled.

Concluding Remarks

The prevention of electrical discharges in hydrodynamic thrust bearings is crucial to avoid babbitt pitting on thrust pads, so as not to result in operational limitations and increased maintenance costs on the unit. Regularly checking the generator's grounding system and measuring shaft voltage are essential preventive measures.

An investigation was conducted on the temperature rise problem in the main thrust bearing of gas turbine unit 3 at Urmia CCPP. It was discovered that all thrust pads had suffered electrical pitting damage caused by shaft current discharge through the bearing. Repairing the generator's grounding system effectively controlled the stray currents and prevented further damages to the thrust pads.

Experiencing bearing damages due to electrical arcing in oil films is not a recent issue; but it can be very challenging to convince power plant operators that such electrical discharges are taking place in the bearing and that they could be the main cause of bearing failure. This is especially true since the evidence of that in the bearing gets erased as the babbitt surface is wiped away in the self-destruction cycle. Many previously unexplained damages and high thrust temperature problems in gas turbine bearings may be attributable to these electric discharges.

References

[1] T. H. McCloskey. *"Troubleshooting Bearing and Lube Oil System Problems,"* Proceedings of The Twenty-fourth Turbomachinery Symposium, pp. 147-166, 1995.

[2] *"A General Guide to the Principles, Operation and Troubleshooting of Hydrodynamic Bearings,"* Kingsbury Inc., pp. 20-21.

[3] *"Stray currents can damage turbine bearings,".* Clarion Energy Content Directors, 1997.

[4] *"Check of Insulation against shaft currents,"* Ansaldo Energia Technical Document, pp. 157-163.

3

High Pressure Centrifugal Compressor Aerodynamic and Mechanical Design - Case Study

Amini, Tayebeh
Abdollahi, Elyas
Rahnama, Farhad
Sadeghi, Borhan
Ghobadi, Mohsen
Ghaseminezhad, Ali
Pourtaba, Hamidreza
Bakhshizadeh, Mohamad

MAPNA Turbine Engineering & Manufacturing Co. (TUGA)

Introduction

Centrifugal compressors are widespread turbomachines in energy industry that can be used to provide the driving energy for gas pressure boosting. This is particularly useful for cold seasons when gas demand grows and there is insufficient level of gas supply and as a result, it is necessary to store gas in hot seasons by injecting it into underground reservoirs. In this regard, MAPNA Turbine, with years of invaluable experience in design and manufacturing of different types of centrifugal compressors for refineries and gas boosting stations, is working on a design project for new injection compressors.

Major differences between this project and previous typical compressors are higher rotational speed (up to 13380 rpm), higher discharge pressure (up to 350 bar), and tandem configuration of compressors (low pressure and back-to-back high pressure) which make them strongly prone to instability.

This article reviews the aerodynamic and mechanical design process of these compressors consisting of conceptual and detailed design. Part of the results is briefly discussed while other items such as thrust force calculations, design of inter-stage seals, cross-coupling forces, optimization, detailed mechanical design based on international engineering codes, thermal analysis, fracture mechanics calculations, and similar mechanical design concerns are not included in this article. Mechanical design discussions are summarized in the impellers and high-pressure casing sections. Other components are excluded and are to be discussed in the later issues.

Aerodynamic Conceptual Design

Conceptual design is the first step of compressor aerodynamic design, which includes initial estimation of overall parameters of the compressor, namely rotational speed, overall dimensions of the casing, required power, number of stages, type of casing, and layout. The conceptual design results are inputs for determining the characteristics of the compressor in order to provide technical and financial proposals.

The working scope of MAPNA Turbine for manufacturing centrifugal compressors is listed in Table 1. Accordingly, conceptual design of compressors within the range reported below is accomplished by internally developed software, the algorithm of which is explained later.

Table 1- MAPNA Turbine's scope of work in centrifugal compressors design

Parameter	Lower limit	Upper limit
Performance Data		
Actual inlet flow, m³/h	600	350000
Discharge pressure, bar	>1	350
Pressure ratio	>1	6
Molecular weight	14	46
Machine Specifications		
Number of stages	1	9
Speed, rpm	-	14500
Impeller/diffuser blade geometry	2D-3D	
Nominal power consumption, MW	0.2	55

■ Conceptual Design Algorithm

The conceptual design inputs are the requirements specified in the compressor datasheet and include at least one operating case with the following information:

1. Gas analysis
2. Inlet temperature
3. Inlet pressure
4. Gas flow
5. Outlet pressure

Regarding the above information, the position of the working point can be located in the classification diagram of compressors (Figure 1). If the operating point is located outside the borderline of centrifugal compressor area, selecting and designing this type is up to the designer's experience for the intended purpose.
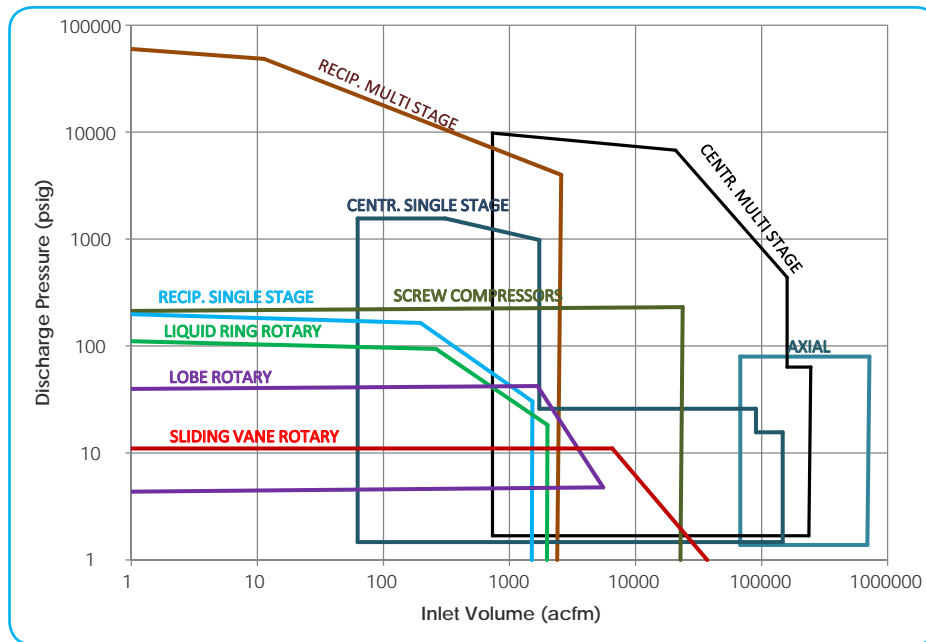
Figure 1- Classification diagram of compressors

Conceptual design algorithm can be seen in Figure 2. It should be noted that assumptions are taken into consideration in different steps of the algorithm based on the case study and the designer's experience.
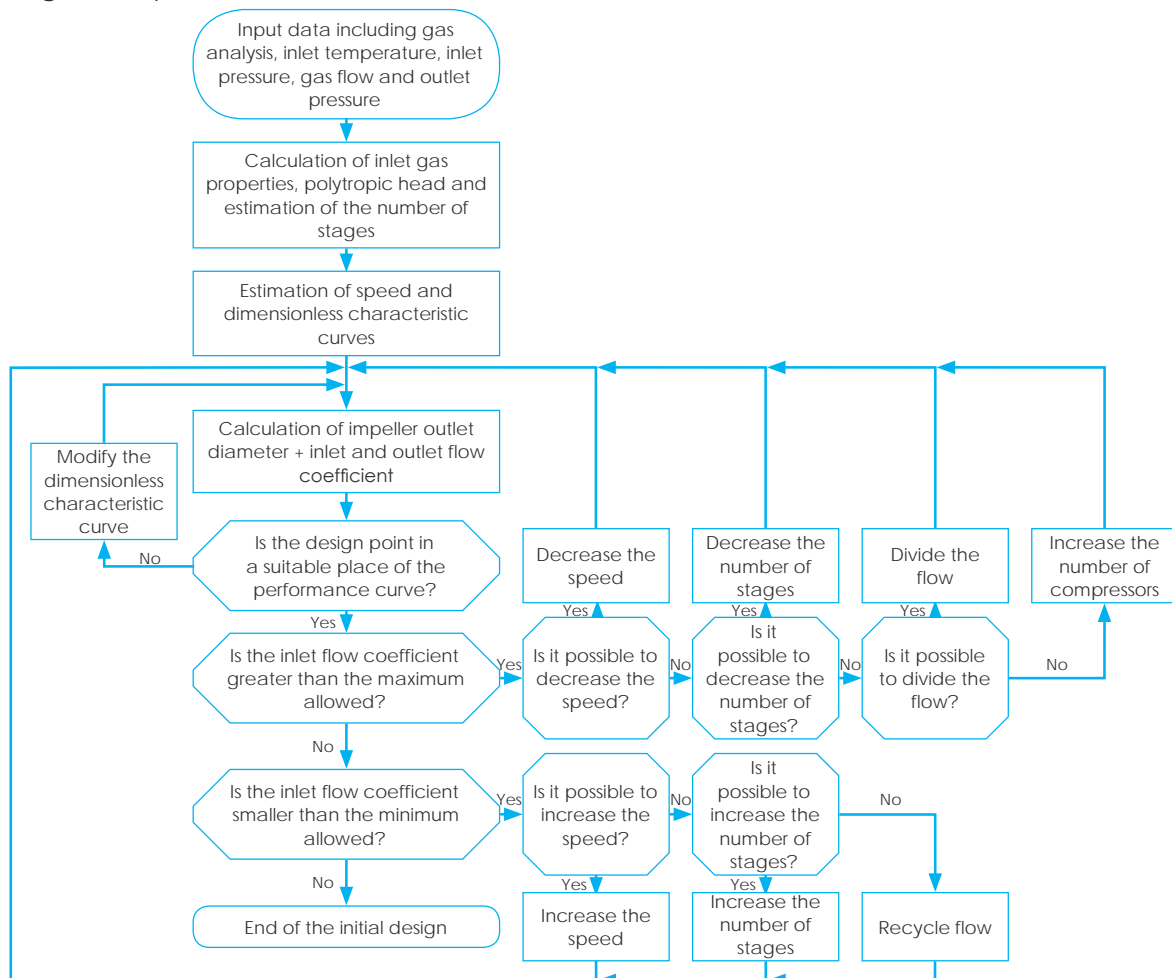

Figure 2- Conceptual design algorithm

■ Conceptual Design

Below is an example of the conceptual design of gas injection project with the following specifications:

Table 2- Conceptual design inputs for case study

Parameter	Values
Weight flow (kg/h)	105605
Inlet pressure (bara)	133.7
Inlet temperature (°C)	57
Outlet pressure (bara)	324
Component	Mass Fraction (%)
CH_4 (C1)	97.488
C_2H_6 (C2)	1.2247
C_3H_8 (C3)	0.1815
C_4H_{10} (C4)	0.1957
C_5+	0.8713
N_2	0.0172
CO_2	0.0216

In the conceptual design, the general characteristics of the compressor, including the number of stages as well as the number of input and output paths are accurately determined. Other parameters, such as impeller outlet diameter, rotational speed, power consumption of the compressor, etc. are also roughly determined, but will be partially modified in the detailed design. Also, initial performance curves are obtained. The dimensionless characteristic curves of the compressor after the conceptual design loop are shown in Figure 3.
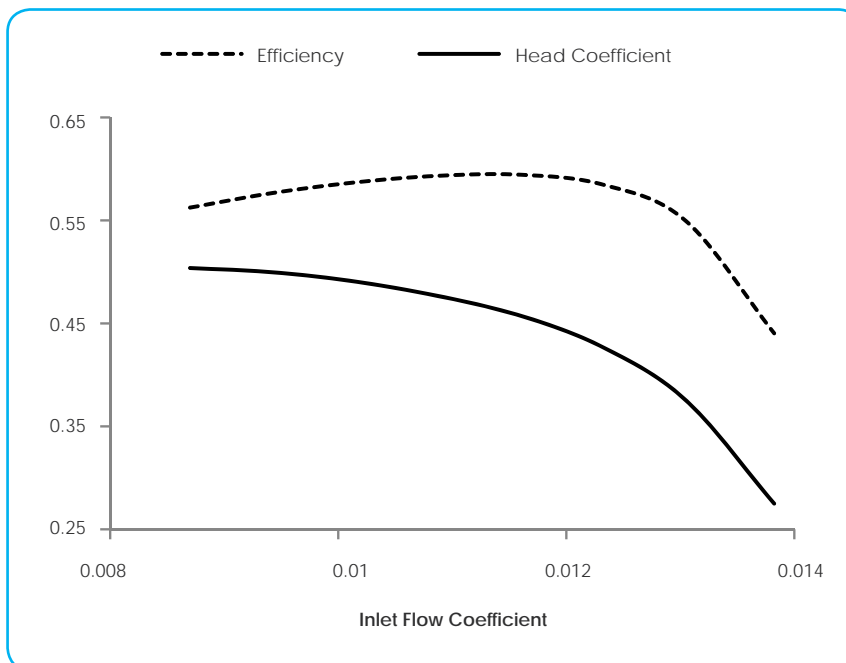

Figure 3- Non-dimensional curves of conceptual design

The important parameters of conceptual design output are reported in Table 3.

Table 3- Conceptual design outputs

Parameter	Conceptual design
Number of stages	6
Speed (rpm)	12500
Efficiency (%)	59.41
Impeller outlet diameter (m)	0.38
Gas power (kW)	8335
Polytropic head (kJ/kg)	169
Discharge temperature (°C)	170

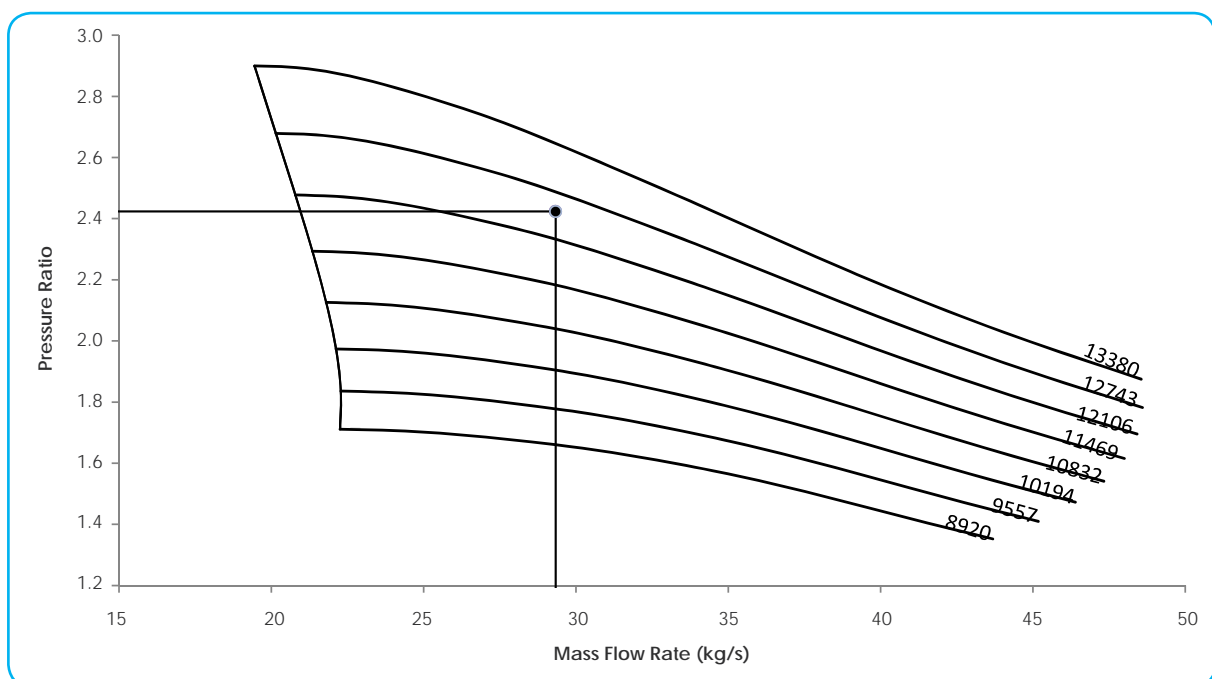Figure 4 illustrates the pressure ratio diagram obtained from the conceptual design.

Figure 4- Pressure ratio curve obtained from conceptual design

Aerodynamic Detailed Design

After checking the technical and financial details of the project with the customer, detailed design gets started. As mentioned, the dimensions of the flow path are not calculated in the conceptual design and only the approximate diameter of the casing is obtained. To attain these details, the following algorithm is used in a commercial piece of software used in the detailed design.

■ Detailed Design Algorithm

The inputs of this stage include the same inputs of the conceptual design in addition to the conceptual design outputs, including the number of stages, rotational speed, and diameter of the impellers. Feedback received from the mechanical design, including structural

considerations, rotor dynamic, as well as production methods and limitations also play a role in detailed design, but to avoid complexity, a simplified algorithm is used. For example, the number of impeller blades cannot be greater than a certain limit, which depends on the manufacturing method and aerodynamic analysis regarding the characteristics of the flow in the channel between the blades which is excluded from this algorithm.

Detailed design algorithm is given in Figure 5. The design of the compressor is carried out stage by stage. After all stages are designed, the final output pressure is compared with the desired value. If the pressure is lower or higher than the desired output pressure, parameters such as rotational speed, impeller output diameter, number of impeller blades, etc. are changed based on the experience of the designer.
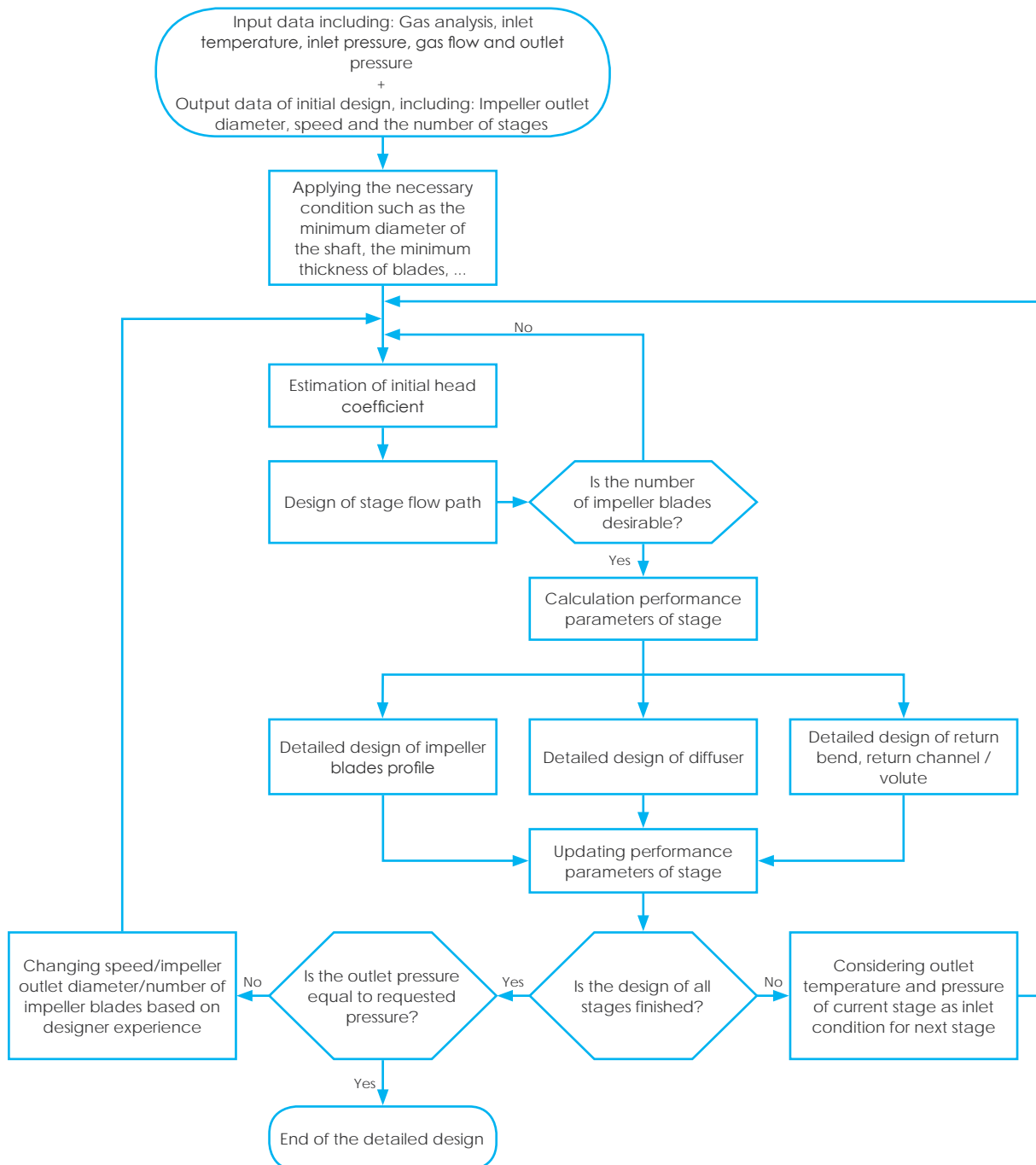

Figure 5- Detailed design algorithm

■ Detailed Design

The outputs of this design include the flow path of the compressor consisting of impellers, diffuser, return bend, return channel, and volute. Impeller blades and return channel vanes are also designed.

The outputs of the detailed design of the mentioned project for the parameters of Table 3 are given in Table 4:

Table 4- Detailed design outputs

Parameter	Detailed design
Number of stages	6
Nominal speed (rpm)	12530
Efficiency (%)	61.6
Impeller outlet diameter (m)	0.383
Gas power (kW)	7997
Polytropic head (kJ/kg)	168
Discharge temperature (°C)	166.5

In the conceptual design, the dimensional information of the flow path is not obtained, but this information is fully acquired in the detailed design. After completing the algorithm and designing all the stages, the overall flow path of the compressor is obtained (Figure 6).
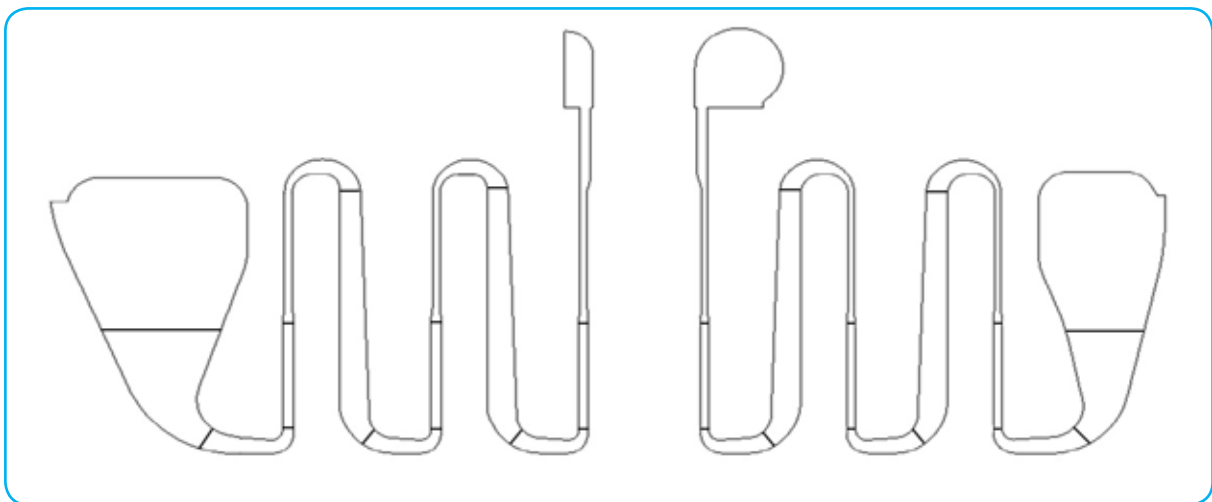

Figure 6- Flow path of all stages

Moreover, Figure 7 depicts the pressure ratio curve of the compressor obtained from the detailed design. It can be observed that the position and slope of the surge and choke lines as well as the operating range of the compressor have changed compared to the conceptual design.
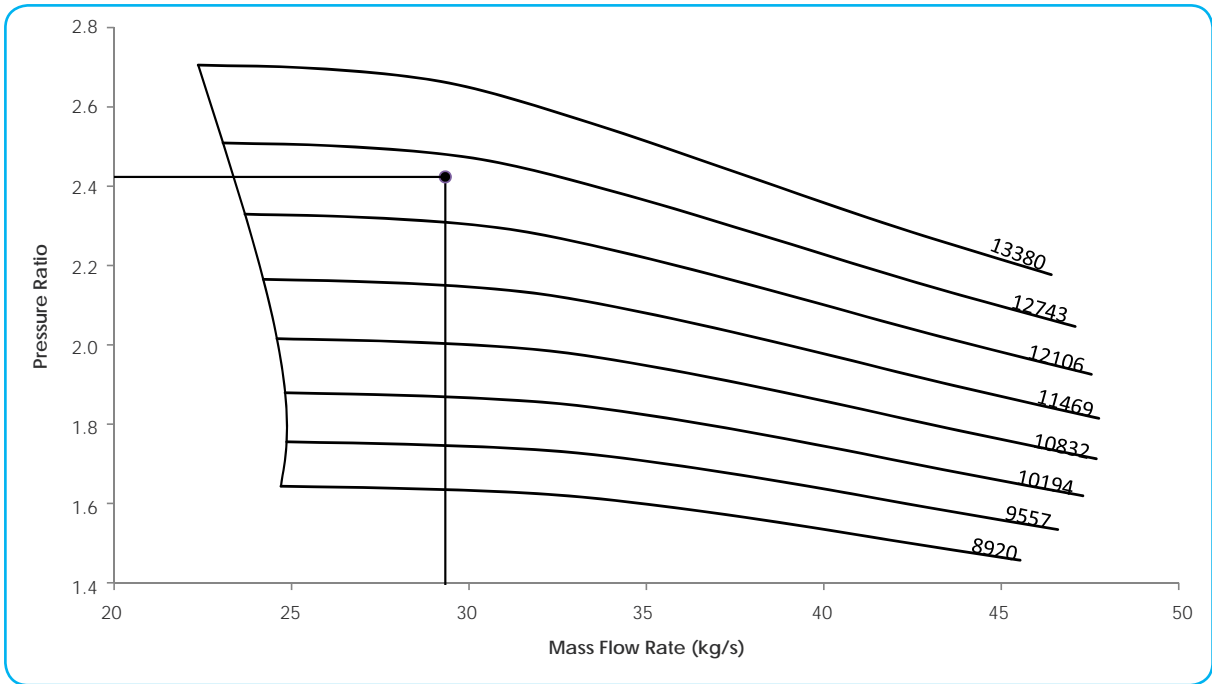
Figure 7- Pressure ratio curve obtained from detailed design

Some of the detailed design outputs, including polytropic head coefficient and polytropic efficiency related to the first stage components in terms of the inlet flow coefficient, are respectively illustrated in Figure 8 and 9.
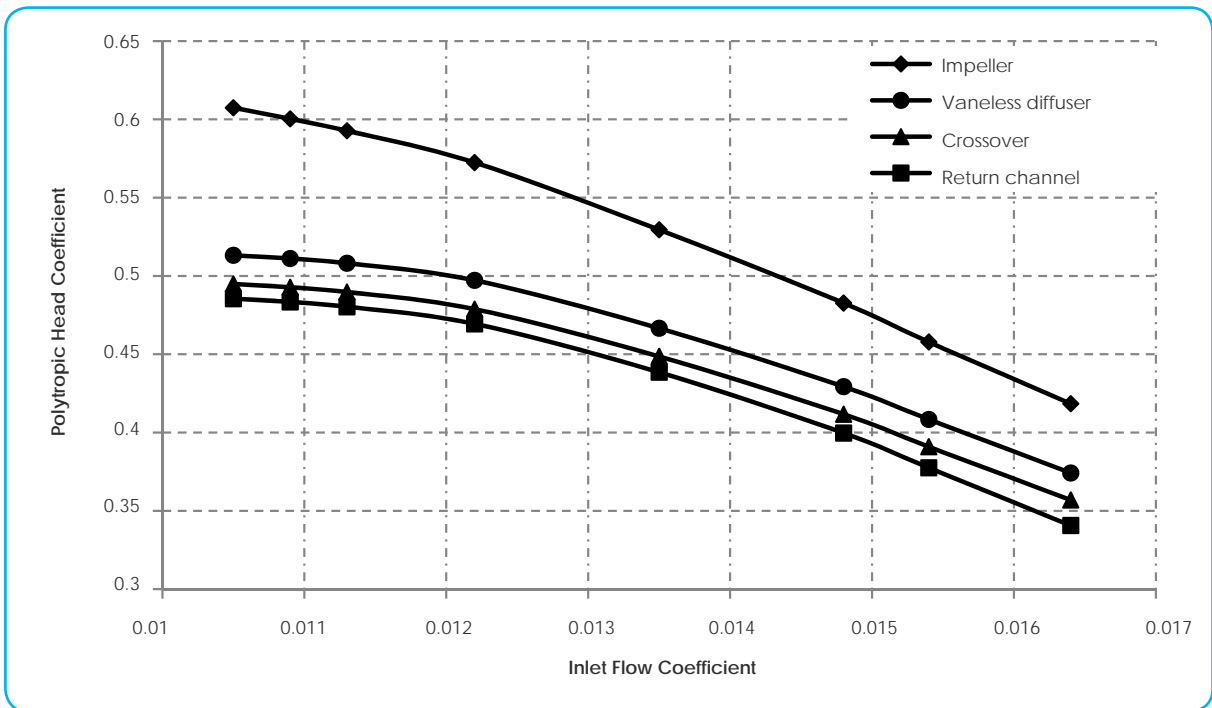

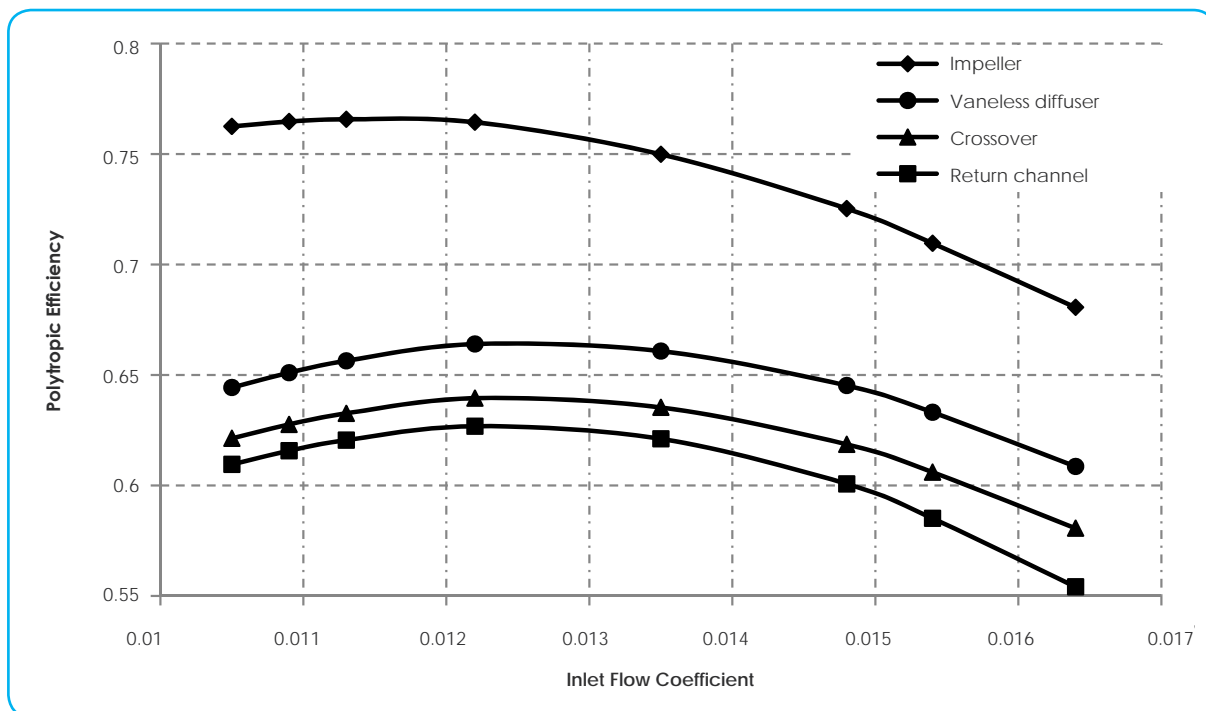Figure 8- Polytropic head coefficient of the first stage components

Figure 9- Polytropic efficiency of the first stage components

Mechanical Design

Based on aerodynamic analysis, flow path result is recurrently commented on and revised by mechanical design and aerodynamic groups, respectively. After flow-path finalization, 3D design of the components (including rotary and stationary parts) is accomplished based on the flow-path sketch. Several considerations need to be taken into account through detailed design in terms of mechanical and thermal stress, high and low-cycle fatigue, elastic and plastic deformations, fracture mechanics, rotor dynamics, stability, etc. All design criteria are adopted from international standards such as API and ASME. Furthermore, feasibility of manufacturing and assembly are two key concerns when confirming the design.

Although mechanical design concept is generally the same for different parts, they are different in both detailed procedure and failure mechanism. In this manuscript, mechanical design of impellers and high pressure casing, as two fundamental case studies of mechanical design of compressor parts will be discussed.

Arrangement of parts around flow path initially focuses on modeling and adjusting sufficient gaps between adjacent parts. According to flow path, compressor cross section is modeled assuming the assembling sequence, inter stage sealing faces and adequate clearance between neighboring rotary and stationary parts. Stationary vanes and rotary blade profiles are also another input data from the aerodynamic analysis.

■ **Mechanical Design of Impeller**

● **Aerodynamic Inputs and Materials**

In order to perform the structural analysis, 17-4PH is selected as base material for impellers in this case study. It is noteworthy that cover disk and main disk of impellers (two main constituents of impellers) shall be joined by brazing or welding. Binding strength is a crucial concern in selecting the joining strategy, which will be determined through a mechanical analysis to be explained.

Calculations

Mechanical design procedure faces several challenges. High rotational speed of the rotor is one of the key characteristics of these compressors which is the root cause of other subsequent challenges turning rotor design into such an intricate task. For instance, high maximum continuous speed of about 13380 rpm would instigate an extreme level of stress and plasticity on the impellers. Consequently, welded or brazed joints of main and cover disks of the impellers are highly stressed. As a result, selecting proper material with appropriate weldability, as well as design and joining techniques become critical.

In addition to centrifugal force, impellers undergo a high level of thrust force due to pressure gradient along the stages, which intensely affects impeller-shaft assembly. The impeller-shaft connection is of interfacial type which must withstand the thrust force. The greater the thrust force to be compensated, the stronger the connection needed (tighter tolerance of shaft and main disk inner diameter) and the greater the bearing stress on both shaft and impeller. On the one hand, a loose assembly would not be perfectly able to withstand the axial thrust, and on the other hand, tighter tolerances would intensify the bearing stress as well as bring about troubles in assembly. Hence, a balance between two aforementioned points is mandatory to strike. A solution to the high thrust force was using a screw-pin mechanism for fixing the impellers on the shaft. But, it would lead to high stress concentration in the impellers' pin hole.

Impellers Finite Element Analysis (FEA)

Interference with shaft and rotational speed are two major sources of stress on impellers. When an impeller is installed on a shaft (zero speed), it is highly stressed due to shrink fit interference. As the rotor speed increases, centrifugal forces induce additional stresses on impellers while the interference stress decreases. Other sources of stress such as working fluid static pressure around and dynamic pressure inside the impeller blades were investigated. However, flow effect is negligible compared to centrifugal and interference stresses.

In order to consider the effect of interference, stress analysis of the impellers was carried out in presence of the shaft. Analysis encompassed four different operational conditions. In the first step, only the interference was considered with no rotational speed. In the second and third steps, the impeller was assumed to rotate with minimum allowable and maximum continuous speeds. The forth step considered the maximum trip speed.

Complexity of the model and thickness of vanes and disks led to new challenges in terms of mesh generation and finite element (FE) solution convergence. To overcome the problem of FE solving time, only one seventeenth of the model was introduced tapping into the cyclic symmetry of the geometry. It should be noted that number of vanes (17 Vanes) is derived from the SAFTY diagram and the aerodynamic analysis. Since the vanes are curved, the impeller is divided into 17 curved sections and shaft is cut accordingly. Modified model is imported in all FE cyclic symmetry analyses with necessary boundary conditions. This strategy reduces solving time more than 95% in different analyses with the same mesh size.

Since impellers operate under high rotational speed and interference, they will undergo highly localized plastic strains. Firstly, simulations were carried out assuming an initial interference and defining material properties for elastic and plastic behavior. For each interference value, the analysis is repeated and results are examined. Figure 10 depicts stress distribution in shaft and impeller sections. Shear and von-misses stress of joining surfaces were reviewed when deciding the welding method and generating the WPS. Figure 11 shows stress distribution in contact between main and cover disk.
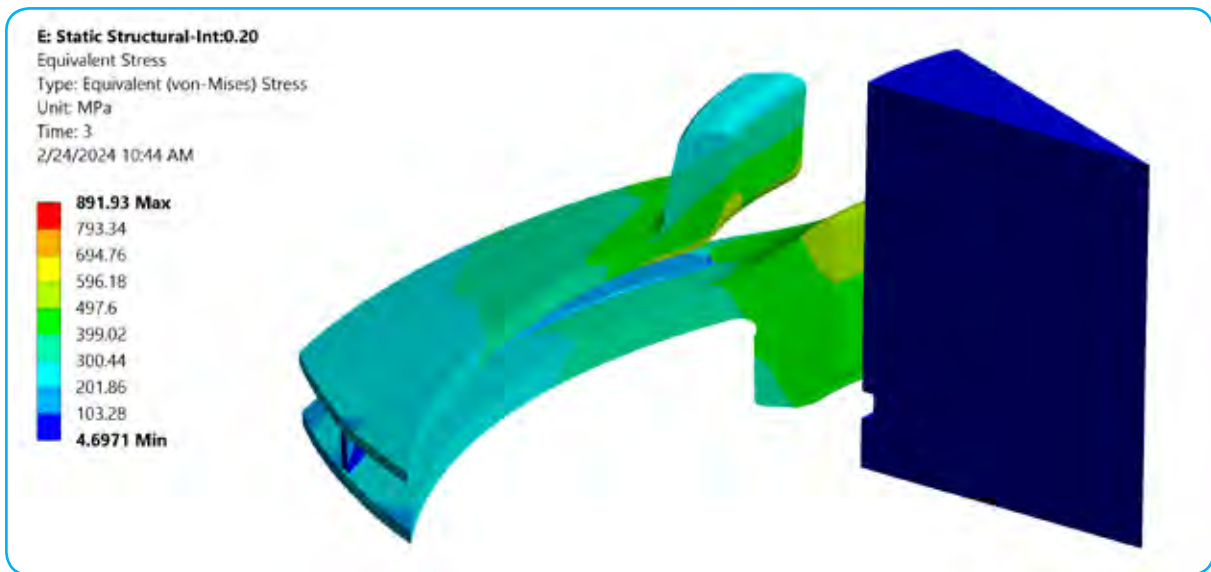
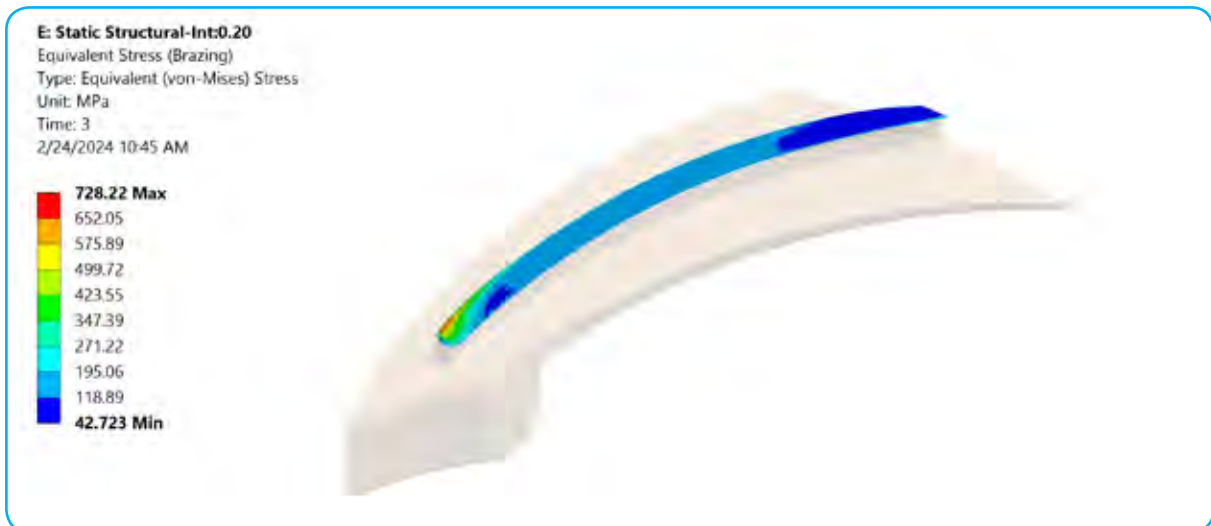Figure 10- Stress distribution in impeller and shaft segment

Figure 11- Stress distribution in main and cover disks connection

- **Life Time Estimation**

Periodic start/stop is quite normal in service condition; therefore, it's important to investigate low-cycle fatigue considering elastic and plastic strains for 17-4PH. Applying Manson-Coffin parameters for the impeller using strain values, low-cycle life was estimated. This analysis is applied for assessing maintenance periods and total life time of impeller considering start/stop cycles. Additionally, heat-treatment cycle of impeller base material was designed in order to increase the low-cycle fatigue life.

- **Interference Calculations**

In determining shaft-impeller interference, there are some constraints limiting the use of extreme values. As mentioned, increasing the shaft-impeller interference generates high stress in impellers and cover and main disk joint. Besides, decreasing the interference disrupts functionality. For the sake of optimization, numerous analyses were conducted with variable

interference values with 0.01mm increments to assess structural strength of impeller. In Table 5, stresses in main disk hub and safety factors is presented.

Table 5- Stress and safety factor in impeller hub after fitting and trip speed

	Operation	Interference (radial)									
		0.16	0.17	0.18	0.19	0.2	0.21	0.22	0.23	0.24	0.25
Von mises stress (MPa)	After fitting	358	380	403	425	447	470	492	514	536	557
	Trip speed	560	554	548	544	540	539	540	551	570	592
Safety factor	After fitting	2.40	2.26	2.13	2.02	1.92	1.83	1.75	1.67	1.60	1.54
	Trip speed	1.54	1.55	1.57	1.58	1.59	1.60	1.59	1.56	1.51	1.45

It must be noted that impellers are assembled on the shaft by heating, resulting in thermal expansion of inner diameter of impeller. By increasing the interference, higher temperature is needed for preheating impellers during assembly, imposing another restriction. Therefore, permissible temperature rise of impellers' material and also temperature loss (due to ejection from the furnace to assembly) defined the maximum achievable interference allowed for impeller-shaft assembly. All these restrictions were calculated and optimized to apply the proper interference between the impeller and the shaft.

● **Close Gap Calculations**

In addition to stress analysis, directional deformation of the impellers in close-gap zones is calculated in different directions through several steps from zero to trip rotational speed. This calculated deformation was added on top of that induced by thermal expansion and dynamic forces. Design of close gaps was done based on these calculations considering interaction between aerodynamic and mechanical design teams to optimize the seal losses and risk of the rotor touching the stationary parts.

● **Frequency Analysis**

Impellers' natural frequency plays an important role in axial vibration resonance prevention as lateral vibration modes were not excited and axial vibration was the dominant mode within the operational velocity range of the rotor. This vibration exposes impellers to high-cycle fatigue stresses which is destructive and may cause mechanical failures. For impellers, natural frequencies were calculated using finite element model described previously. In Figure 12, Campbell diagram for impeller stage 1 (for example) is depicted with different harmonic indices. As can be seen, passing vane frequency intersects the impeller's natural frequency in compressor working range, which excites high amplitude vibrations in exterior edge of the impeller. To overcome the high-cycle fatigue failure in these areas, scalloped cutouts were made on impellers to remove high amplitude vibration regions. This modification moved the location of peak vibration to a stiffer area on the impeller. Figure 13 demonstrates the vibration mode shape for non-scalloped impeller and scalloped impellers.
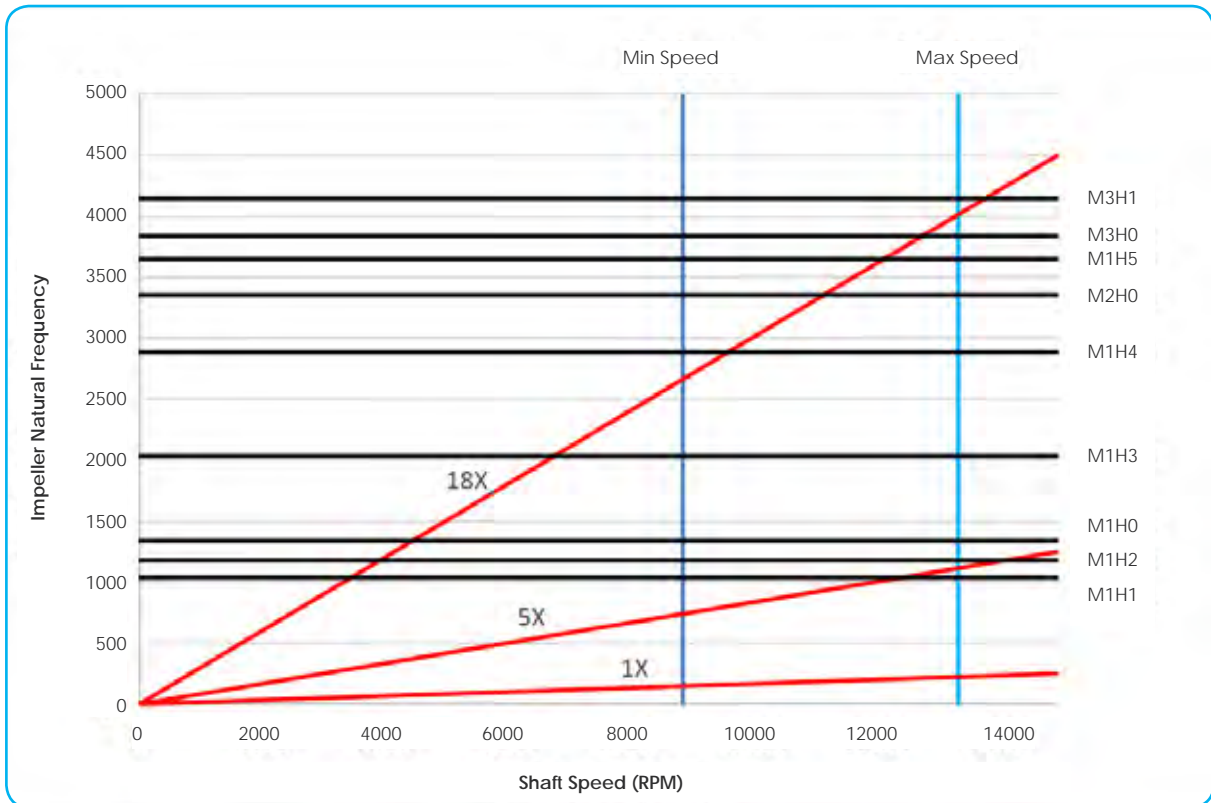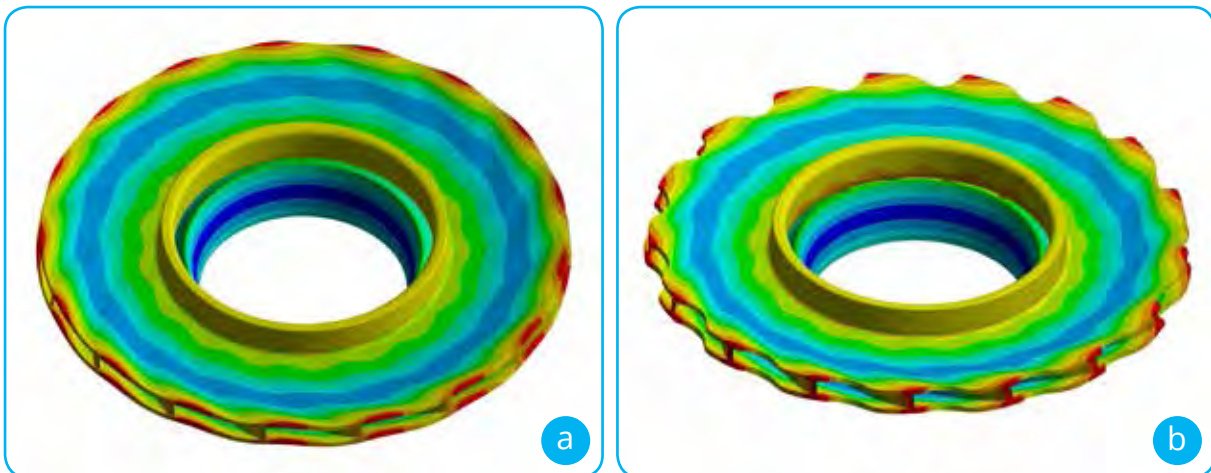
Figure 12- Campbell diagram for impeller stage 1

Figure 13- Vibration mode shape for (a) non-scalloped impeller and (b) scalloped impeller

■ Mechanical Design of Casing

Based on API 617, allowable tensile stress of pressure casing should not exceed 25 percent of minimum ultimate tensile strength of the material at maximum specified operating temperature. Also, it is allowed to design casing with the aid of finite element analysis, provided that the design limits comply with ASME Code, section VIII, division 2. Accordingly, the primary value of high pressure compressor casing thickness is calculated. Besides, ASME section VIII, division 2, part 5 (DESIGN BY RULE REQUIREMENTS) is applied in order to cover all loadings, geometries, and details. In this regard, finite element simulations were performed to examine the designed thickness with respect to service factors such as maximum and minimum temperature, hydrostatic test pressure, vibration load, thermal load, and unexpected loads (like earthquake).

The design-by-analysis requirements are organized based on protection against the following failure modes:

1. Protection against plastic collapse

2. Protection against local failure

3. Protection against failure caused by cyclic loading

To perform accurate stress analysis considering four different failure modes, material properties including physical properties, strength parameters, monotonic stress-strain curve and cyclic stress-strain curve were determined for the selected base material. All applied loads and load case combinations were considered in the analysis.

● Casing Finite Element Analysis

In order to simulate all applied loads considering the effects of non-linear geometry, a 3D model was developed. Figure 14 demonstrates von-misses stress results of FEA at critical zones. In the FE calculation of the casing, thermal stress is as dominant as mechanical stress. Hence, both types must be simultaneously taken into account. Temperature distribution of the casing is also illustrated in Figure 15.
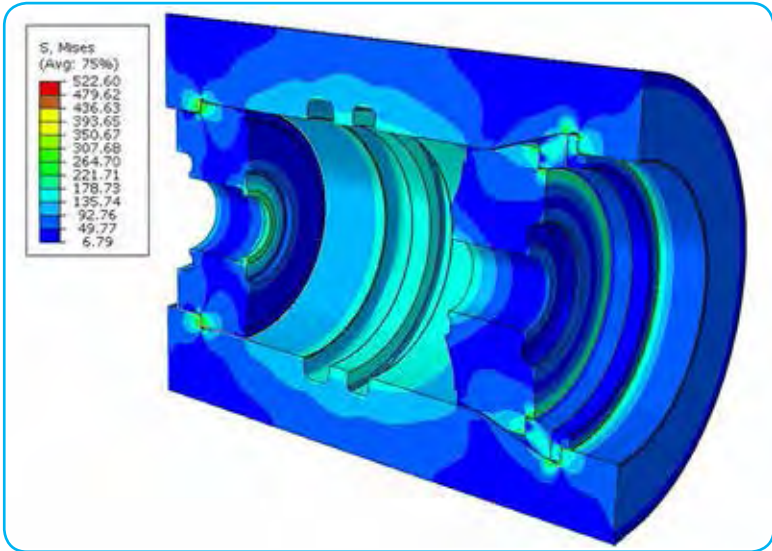

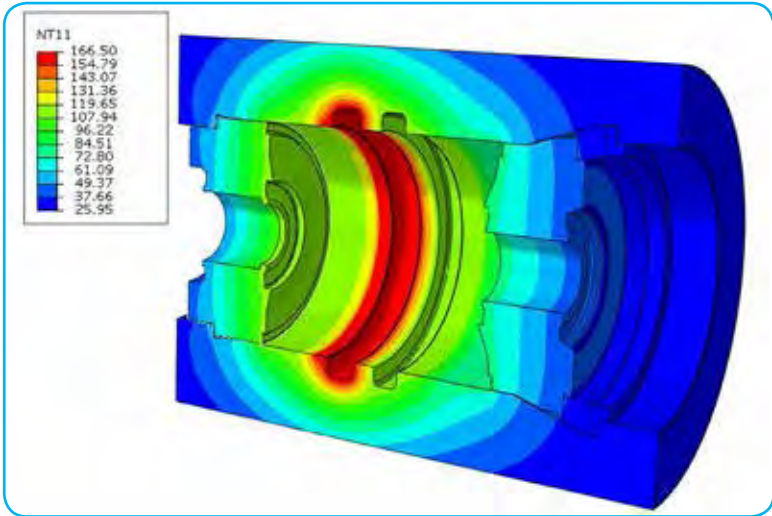Figure 14- Von-misses stress results of high pressure casing

Figure 15- Temperature distribution of the high pressure casing

As the casing was designed for twenty years of service life, life limiting factors were accordingly optimized:

- **Protection Against Plastic Collapse**

Considering the complex geometry of the casing and complications regarding Elastic Stress Analysis method such as stress categorization (membrane, bending, and peak stress), the elastic-plastic analysis method was implemented. According to 5-step assessment procedure, the casing was numerically analyzed and the convergence of the calculation verified that the casing was protected against plastic collapse.

- **Protection Against Local Failure**

In addition to plastic collapse criteria, local failure was the next concern that had to be checked. ASME obliges an elastic-plastic stress analysis as the method for local failure investigation. Following the ASME recommended procedure, the strain limit lay within the acceptable limit and local failure criteria were satisfied as well.

- **Protection Against Failure Caused by Cyclic Loading**

In order to control fatigue and the ratcheting due to cyclic loading, elastic-plastic stress analysis and equivalent strains method was deployed. Based on the obtained FEM result, there was an elastic core in the primary load-bearing boundary of the component and so the ratcheting criteria were satisfied. Also, computing the accumulated fatigue damage using the 10-step criteria, the damaged zone was located in the safe region of the casing.

Concluding Remarks

This article outlined the latest achievements of MAPNA Turbine in the field of aerodynamic and mechanical design of centrifugal compressors with high rotational speed (up to 13380 rpm), high discharge pressure (up to 350 bar), and tandem configuration of compressors (low pressure and back-to-back high pressure) which made them strongly prone to instability.

Aerodynamic design, as the first step to design these compressors, was explained in two steps of conceptual design and detailed design. The outputs of this design were used as the input for the subsequent design stages.

Regarding the mechanical design, calculations associated with the impellers and high pressure casing - as the most important rotary and stationary parts - were presented. For the impellers, numerical analyses were conducted in four rotational speeds to investigate fatigue (low and high-cycle) and obtain the proper impeller-shaft interference. To design the impeller in plastic zone, a new approach was adopted in which only 1/17 of the whole geometry was simulated, greatly decreasing computational costs and time intervals. Moreover, a proper close gap was chosen to minimize efficiency loss and prevent any touch between rotor and stationary parts. Finally, frequency analysis was performed to prevent impeller resonance and increase high-cycle fatigue life time by modifying the exterior edge. Mechanical design of high pressure casing was another topic discussed. Stress and temperature distribution analyses were conducted, and the results as well as the ASME code acceptance criteria were briefly discussed. All ASME requirements were successfully satisfied ensuring reliable functionality of the impellers and the casing.

Capability to design and manufacture these high-pressure centrifugal compressors further enriches MAPNA Turbine's product portfolio and creates value for costumers, specifically in cold seasons when gas demand grows.

Introduction

Correct prediction of an internal combustion engine's performance depends on the accurate modelling of its individual subsystems. Turbocharger is one of the components directly affecting the power-to-weight ratio of engines, an inaccurate model of whose performance would lead to deviation from the intended actual engine performance. Estimating the turbocharger's map can be achieved through experimental tests, as well as analytical or numerical methods. In early stages of product development, a restricted test-only approach necessitates a series of prototyping, which incurs substantial costs. The similarity solution approach on the other hand, provides an estimation of the turbocharger performance, contributing to reduced costs. Following the similarity solution, performance map can be achieved swiftly using computational fluid dynamic (CFD) calculations and at a comparatively lower cost than that required for prototyping and test execution. This article outlines the details of the CFD approach that brings about significant reduction of calculation time and acts as a reasonably accurate asset in product development.

4

A cost-efficient CFD approach to attain turbocharger compressor performance map

Sepehri, Emad
Rajabi, Emad

*MAPNA Turbine Engineering & Manufacturing Co. (TUGA)*
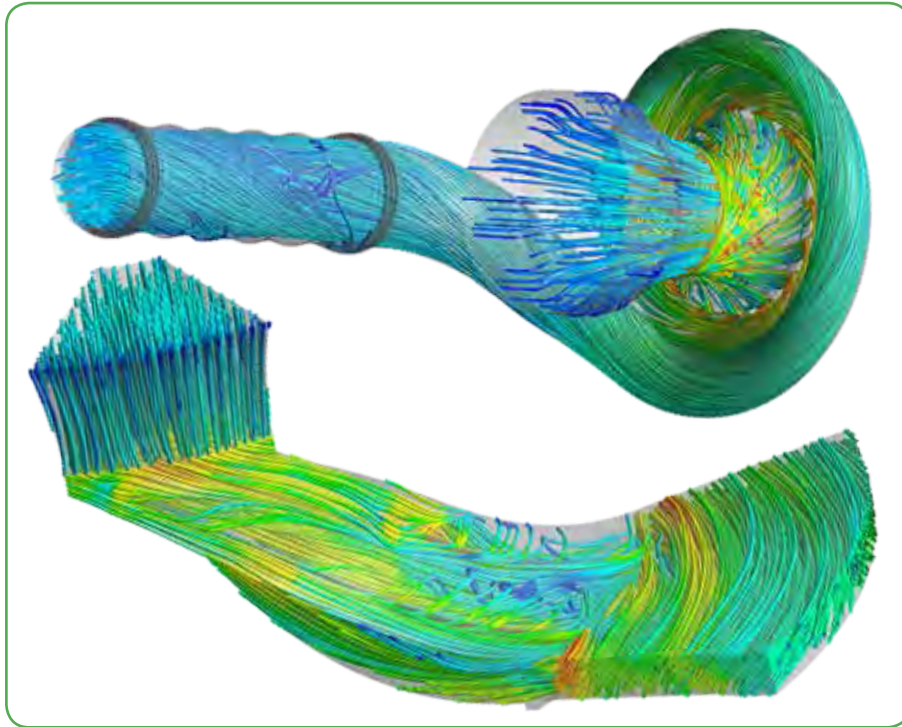
Computational Domain

The compressor map serves as a comprehensive guide providing valuable insights into critical parameters such as turbo spool speed, boost pressure, mass flow rate, and compressor efficiency across diverse operational scenarios. The surge and choke lines emerge as pivotal demarcations of operational boundaries of compressors. The surge line determines the lower limit where insufficient gas flow may lead to flow reversion, potentially causing mechanical stress and damage to the device. Conversely, when the choke line is surpassed, the upstream will be isolated from downstream. Achieving the compressor performance map tapping into CFD approaches is beneficial but requires a substantial number of simulations on each speed line, especially in regions close to the surge and choke lines. A preliminary draft of the compressor map requires at least 8 constant-speed rotation lines. This calls for a significant number of simulations, demanding robust computational resources and a substantial time on hand.

In the compressor simulation, two distinct computational approaches come to the forefront: 1) the Periodic Domain, and 2) the Full Domain. A trade-off between computational affordability and accuracy based on the analysis purpose makes it possible to choose from the two options. For purposes similar to the present activity, periodic simulation of a centrifugal compressor offers several advantages over its full domain counterpart. Among these advantages are diminished computational expenses, improved simulation convergence, enhanced observational access to the dynamic phenomena around blades, elevated computational mesh quality, expedited design optimization, and a more thorough understanding of localized flow behaviors. This simulation type is also highly valuable in the middle of design process stages for scrutinizing local flow dynamics, performance issues and modular redesign. However, its efficacy relies on the assumption that the periodic segment accurately represents the flow characteristics across the entire domain. It's worth noting that under highly unstable or intricate conditions, this approach may introduce some level of error in compressor map estimation. On the other hand, full domain CFD simulations provide a more accurate representation of flow features, enabling a detailed analysis of interactions between rotating and stationary components and capturing physical parameter along the compressor volute for optimizing design and ensuring stability. These simulations enable precise prediction of losses, aiding the accurate calculation of compressor efficiency and facilitating optimization of both geometry and operating conditions.

To assess the precision of periodic domain simulation in comparison to the complete domain, four working points were simulated based on engine test data. Table 1 reports the difference between the total-to-total absolute pressure ratio and the total-to-total isentropic efficiency for periodic and full domain simulations. Upon a thorough analysis of the results, it becomes evident that the differences in parameters between the two simulation scenarios are limited to a margin below 6 percent. As depicted in Figure 1, taking into account the volute and the compressor outlet in the full-domain simulation leads to a more significant pressure drop compared to periodic simulations. Therefore, the pressure ratio and isentropic efficiency are higher for periodic domain compared to the full one. Among the advantages of the periodic simulation over the full simulation are:

Increased execution speed - up about four times

RAM   75% less RAM usage

An 88% decrease in total number of computational cells as well as the volume of simulation storage files

Considering the advantages of periodic simulation and its appropriate accuracy, it is logical to utilize this approach for simulations of compressor map.

Table 1- Contrasting key parameters between two simulation scenarios: full domain versus periodic domain

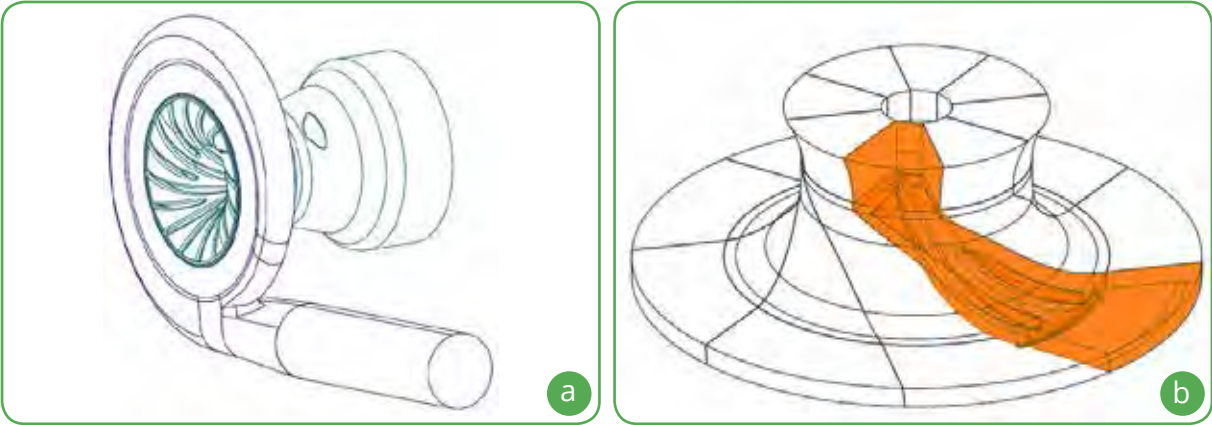| Spool speed	Full domain		periodic domain		Error %
52470.4 rpm	$PR_{t\text{-}t}$	4.31	$PR_{t\text{-}t}$	4.55	5.57
	$\eta_{t\text{-}t}$	76.33	$\eta_{t\text{-}t}$	78.88	3.34
42887.7 rpm	$PR_{t\text{-}t}$	3.12	$PR_{t\text{-}t}$	3.27	4.81
	$\eta_{t\text{-}t}$	80.92	$\eta_{t\text{-}t}$	83.7	3.48
32171.5 rpm	$PR_{t\text{-}t}$	2.05	$PR_{t\text{-}t}$	2.07	0.97
	$\eta_{t\text{-}t}$	82.45	$\eta_{t\text{-}t}$	84.06	1.95
19493.1 rpm	$PR_{t\text{-}t}$	1.32	$PR_{t\text{-}t}$	1.33	0.75
	$\eta_{t\text{-}t}$	83.62	$\eta_{t\text{-}t}$	85.56	2.32

Figure 1- Computational fluid domain a) full domain, and b) periodic domain

Thrust bearings are employed to counteract axial forces applied on turbo spool due to the difference of total drag forces between the turbine and compressor. The details of flow rotation at the impeller inlet significantly impact thrust force calculations, but this has a negligible effect on the results of the performance map. Increasing or decreasing the rotational region at the compressor inlet result in reduction or increase in the magnitude of the thrust force, respectively.

The compressor back plate shown in Figure 2 holds significance in the analysis of heat transfer and compressor sealing but has a negligible effect on the results of the compressor simulation and the magnitude of thrust force. Consequently, it has not been included in the simulations of the performance map.
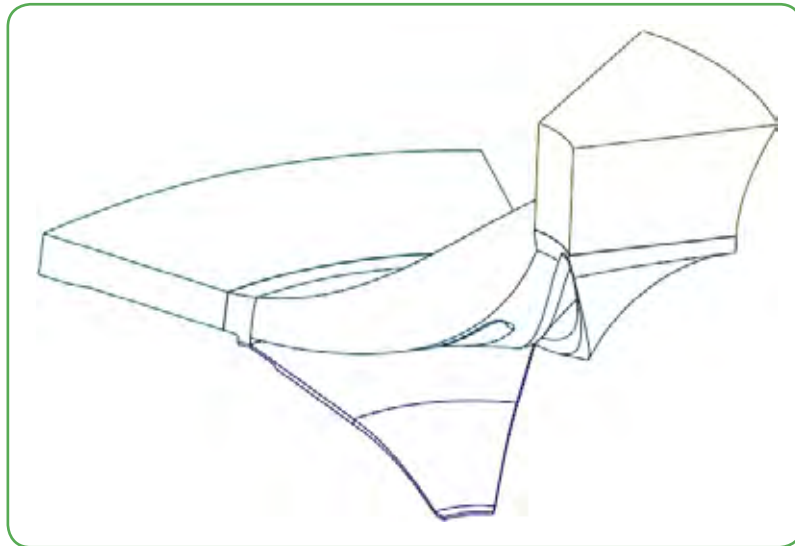

Figure 2- Compressor stage with back plate

Influential Factors on Simulation Speed

The selection of an appropriate solver significantly influences computational efficiency in CFD simulations. Figure 3 depicts the characteristics of the compressor derived from the periodic simulation. Due to the surge phenomenon, solution convergences near the surge line are complicated and speed of convergence decreases. The Coupled method (coupling between velocity and pressure) was used in order to achieve stability and improve convergence speed near the surge area. The algorithm depicted in Figure 4 demonstrates the solving approach for Coupled and SIMPLE methods. The Coupled method adopts an implicit strategy, concurrently and continuously solving the momentum and pressure equations. Consequently, this method experiences an increase in memory consumption while resulting in enhanced convergence. The SIMPLE method, however, is a semi-explicit approach that solves the pressure and momentum equations in a decoupled manner with less memory usage and is used in other compressor working points - far from surge line.
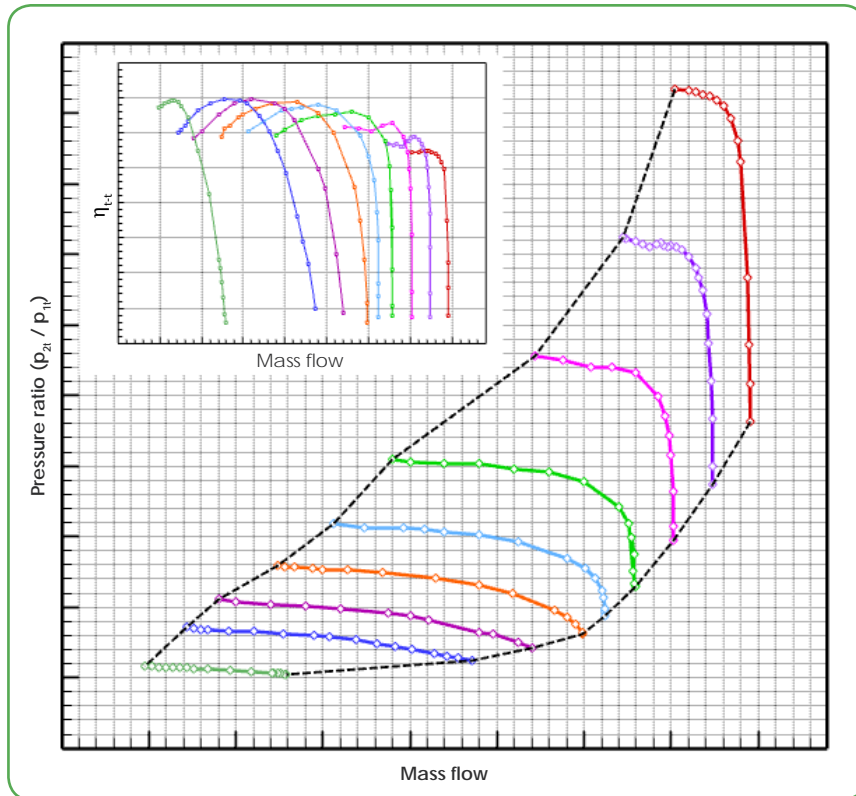
Figure 3- Compressor characteristics

At the outset of the simulation, the solution algorithm assigns the initial values to the solution variables. These values are set close to the approximate final values, bringing about fewer iterations to achieve final results while reducing the run-time and improving the stability. Therefore, it is an effective approach to use the results from cases with lower flow rates or pressures as initial values for cases with higher flow rates or pressures along the progression of each speed line. This tactic expedites the solution and improves robustness.
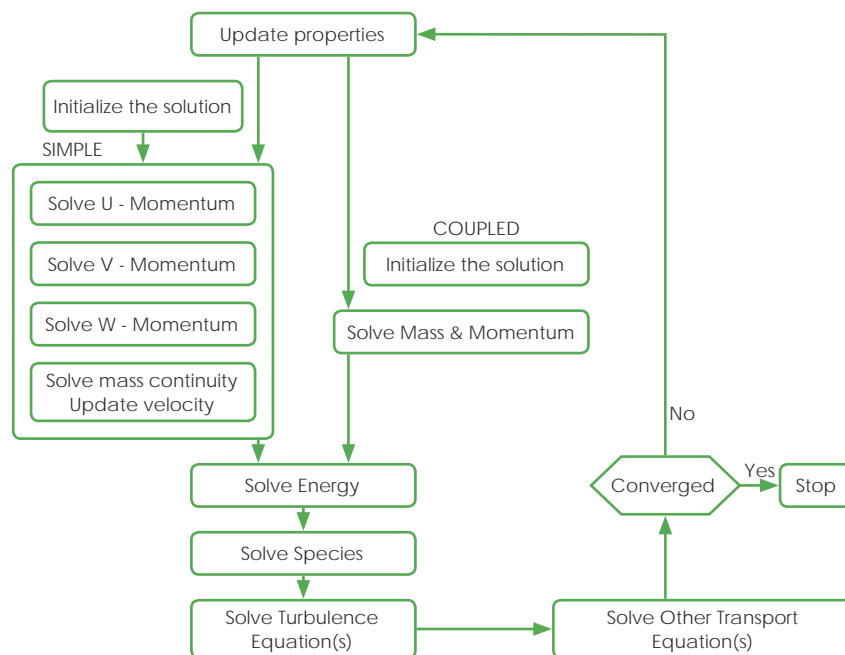

Figure 4- Illustration of the numerical simulation procedure

Hybrid Mesh

Two simulations were conducted periodically to examine the influence of mesh type and quality on compressor characteristic estimation. The configurations for both cases were entirely identical, with the only variation in the volume mesh generation methods: mosaic and tetrahedral. Mosaic meshes incorporate polyhedral elements in boundary layers with prominent gradient changes, contributing to an improvement in mesh quality and solution accuracy. Furthermore, due to the greater number of faces in polyhedral elements compared to tetrahedral ones, false diffusion in numerical solutions decreases, enhancing the representation of flow phenomena and reducing the need for excessive mesh refinement. Compared to the mosaic mesh, the tetrahedral mesh experienced a more than 50% increase in cell count during the assessment of the final mesh results. The simulations for both cases were conducted under same settings. The results revealed an approximate 40% enhancement in simulation speed, a 17% reduction in memory usage, and a significant 30% decrease in output file size when the case adopted the mosaic mesh. This comparative analysis underscores the impact of mesh selection on computational efficiency and resource utilization in technical simulations.

In summary, making use of a mosaic mesh resulted in less overall complexity and more convenient modifications. Furthermore, hybrid meshes can offer improved memory efficiency, making them suitable for simulations with limited computational resources.
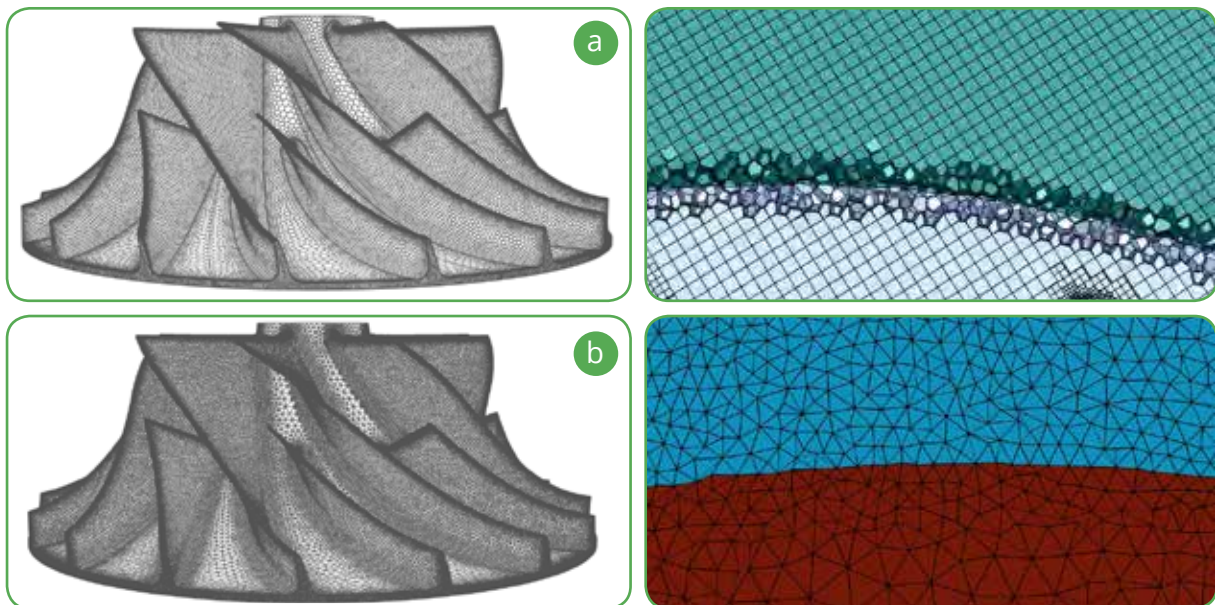

Figure 5- Computational cells:
a) mosaic mesh (Polyhedral + Hexahedral) ,and b) tetrahedral mesh

Concluding Remarks

In this study, an approach to compressor simulations was proposed that resulted in remarkably reduced run time and enhanced computational efficiency. This approach involves:

1. Reducing the computational domain

2. Employing various solvers considering the physical nature of performance points

3. Applying appropriate initial conditions

4. Utilizing a mosaic grid

The cost reduction achieved using this approach makes it possible to estimate the compressor performance map with sufficient accuracy using limited computational resources.

Introduction

Impellers are among the most essential compressor components which are subjected to extreme stresses [1, 2]. Therefore, geometry, material and manufacturing method of these parts are of great importance [3]. In general, there are three methods for production of closed impellers: single-piece, two-piece (the most common), and three-piece. The hub and blades are usually forged, cast or milled, and the shroud is afterwards connected to the hub and blades. The techniques that can be used in the two-piece method are riveting through blades, fillet welding, slot welding, as well as E-brazing, brazing and electroplating. [4]. The ability to join non-homogeneous compounds (including metal-ceramic joints), limited microstructural evolution, relatively high-strength joints, and small Heat Affected Zone are among the advantages of brazing over other methods [5]. High-vacuum brazing method has been more and more accepted over the past few years on account of maximum accuracy and minimum blockage [1].

In this article we shall outline details of the Vacuum Brazing method carried out in MAPNA Turbine for production of impellers with a diameter of around 500 mm and an opening gap of 5 to 8 mm. Different fillers will be evaluated and further tests shall be conducted to ensure the joint brazed with the chosen filler meets the design requirements.

5

An Investigation of Vacuum Brazing for manufacturing 17-4PH Centrifugal Compressor Impellers

Rastar, Vahab
Moradi, Saeed
Fathi, Alborz
Javadi, MohammadAmin

MAPNA Turbine Engineering & Manufacturing Co. (TUGA)

Vacuum Brazing Process

Considering the lack of access to grind the weld root of the impellers being studied, the only method to make such impellers is the brazing process.

Vacuum Brazing is a process that creates high quality joints in a vacuum atmosphere. As can be seen in Figure 1, when manufacturing blades using vacuum brazing, filler metal is placed between the blade and the cover. The impeller prepared for brazing is then placed into a special furnace where brazing is performed [7]. The principle temperature and pressure patterns for this process are shown in Figure 2. In this process, the vacuum of 10-4 mbar serves not only to prevent oxidation of surfaces, but also to clean these faces from any soiling by evaporation and to activate them for wetting by the brazing alloy. The melted brazing metal joins the two faces by both bonding, as well as penetration of "brazing alloy" and "steel" into each other through diffusion, resulting in a particularly strong connection.
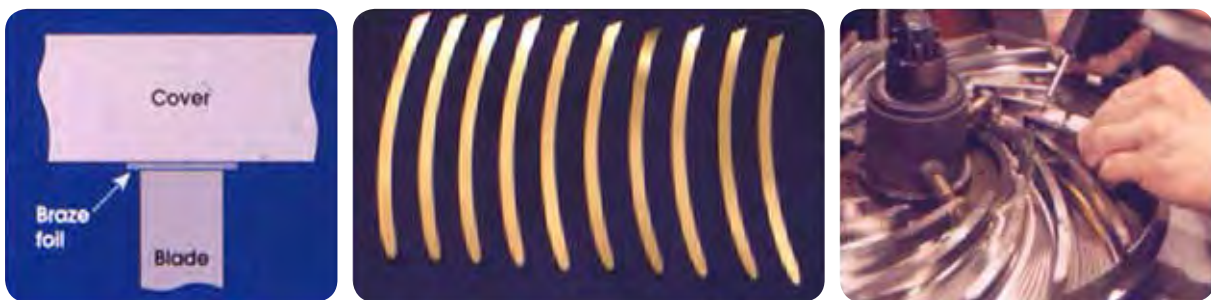

Figure 1- Producing an impeller by brazing [7]

Owing to the computer control of the brazing process, the quality of the manufactured impeller is practically independent of the operating personnel and the percentage of defects is extremely low. Furthermore, experiments show that brazed connections properly maintain their strength at high rotational speeds. Although there are no physical limitations for application of the brazing process, it requires a very precise dimension matching and coordination between the top of the blades and the surface of the hub or shroud that is supposed to be connected to them. If the gap is too large, the connection will be weakened and the shroud or hub will be separated from the blade. Therefore, a gap of 50 to 100 microns is required for the process, necessitating pre-treatment of the material and a process control to ensure that no deformation occurs. This automatically leads to superior geometrical quality of the impellers, which meets the highest accuracy requirements. [3, 6].
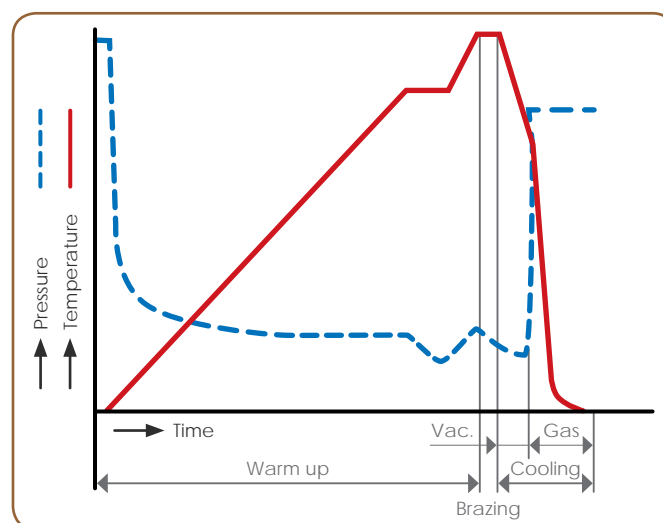

Figure 2- Temperature-time and Pressure-time curves for brazing of an impeller [6]

Although brazed joints have many favorable features, the strength of this connection will falter if brittle intermetallic phases are created due to elements like boron, phosphor or silicon which are added to the brazing alloy to lower the melting temperature,. Consequently, choosing the suitable brazing alloy is of utmost importance in brazing [6].

Choosing the Proper Filler

The material of the impellers being studied, is a martensitic precipitation hardened stainless steel, type 17-4PH [8]. These martensitic stainless steels can be hardened by quenching from the austenitizing temperature (around 1040°C) and then aging between 480 to 620°C. Since these steels contain less than 0.07% carbon, the martensite is not very hard and the hardening is obtained from the aging (precipitation) reaction [9].

Chemical composition of 17-4PH alloy is shown in Table 1. As can be seen, this steel contains about 4% copper. The presence of copper in this steel results in formation of nonmetric copper-rich precipitation that gives it the required hardness and strength. Depending on the temperature of the aging heat treatment, different mechanical properties can be obtained from this steel. Table 2 shows the different conditions of aging heat treatment and the resulting strength and hardness for this alloy [8].

Table 1- Chemical composition of 17-4PH alloy [8]

UNS No.	%C	%Cr	%Ni	%Mo	%Nb	%Ti	%Cu
S17400	0.07	15 - 17.5	3 - 5	-	0.15 – 0.45	-	3 - 5

Table 2- Aging condition of 17-4PH alloy [8]

Condition	Temperature (°C)	Time (Hour)	Tensile Strength (MPa)	Yield Strength (MPa)	Hardness (HRC)	Impact Energy (J)
H900	482	1	1310	1172	40- 47	-
H925	496	4	1172	1069	38 – 45	7
H1025	552	4	1069	1000	34 – 42	20
H1075	579	4	1000	862	31 – 36	27
H1100	593	4	965	793	30 – 37	34
H1150	621	4	931	724	28 - 35	41

Although brazing is a conventional process for joining steels, it is difficult to join 17-4PH alloy as its mechanical and metallurgical properties may change due to heating and cooling during brazing cycles. As a result, the characteristics of filler and brazing cycle should be selected in such a way that this alloy undergoes minimum metallurgical changes. Through preliminary studies, it was realized that the best brazing fillers for joining these types of materials are nickel-based, gold-based and sometimes palladium based filler metals [6].

To investigate these fillers, three different foils including BNi-2 (nickel based) [10], BVAu-4 (gold based) [10] and PGK-1000 (palladium based) [11] with a thickness of 50 microns were selected. The chemical composition of these fillers can be seen in Table 3.

Table 3- Chemical composition of the brazing fillers [10, 11]

Brazing Filler	%Ni	%Cr	%Pd	%Au	%Fe	%Si	%B
BNi-2	Rem.	6 - 8	-	-	2.5 - 3.5	4 - 5	2.7 - 3.5
BVAu-4	Rem.	-	-	-	81.5 - 82.5	0.2 max.	-
PGK-1000	Rem.	18 - 20	45.8 - 50	-	-	-	-

For each filler, 3 samples were prepared; one to be cut and investigated by metallography, and the two others to be subjected to shear strength test. The sample surfaces were grinded and washed with acetone in an ultrasonic bath. Afterwards, they were placed in the fixture by a lap joint with an overlap width of 5 mm (Figure 3), and were put in a vacuum furnace with a pressure of 10-3 bar according to the brazing conditions of Table 4. Aging heat treatment was also performed as a post-braze heat treatment. As can be seen in Figure 4, all samples were free of defects.
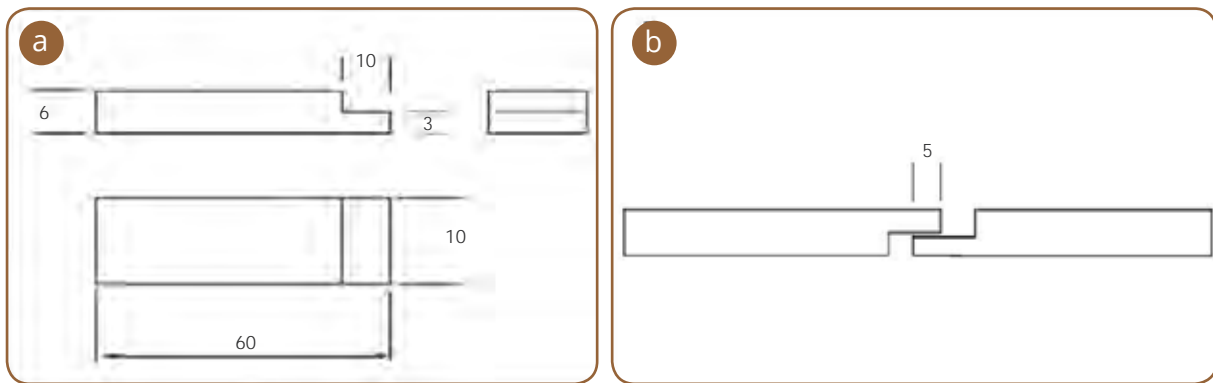

Figure 3- a) Dimension of samples b) Joint preparation

Table 4- Brazing condition of samples

Brazing filler	Brazing temp.	Holding time	Post-braze heat treatment
BNi-2	1050	1 h	
BVAu-4	1050	1 h	Aging condition H1025 (Holding for 4h at 622 °C)
PGK-1000	1260	30 min	

Figure 4- a) Ni based filler (BNi-2) b) Au based filler (BVAu-4) c) Pa based filler (PGK-1000)

In order to compare the strength of the fillers after this specific brazing cycle, the specimens embedded in the fixture were subjected to tensile test and after failure, the shear strength was calculated by dividing the failure force by the cross-sectional brazed area. A comparison of the shear strength results of these fillers (Table 5) reveals that the highest shear strength was obtained when using gold-based filler. However, as a higher strength was expected, the brazing cycle has further optimized to ensure that the base material properties are maintained.

Table 5- Comparison of different brazing filler foils

Brazing foil type	Shear strength (MPa)
BNi-2	308
BVAu-2	565
PGK-1000	493

Evaluation of Joint Properties Using Gold-Based Filler

Since the connection area of the blade to the cover in the impellers is under shear force, it is necessary to evaluate the shear strength of the brazed joints. However, since the brazing cycle was modified, along with the shear strength tests, a brazed sample had to be subjected to a tensile test to evaluate the properties of the base metal. Cylindrical samples were machined with a diameter of 10 mm, and were joined to each other using BVAu-4 foil with a thickness of 100 microns during the cycle shown in Figure 5 in a brazing vacuum furnace of 10-4 bar at a temperature of 1010ºC and holding time of 1 hour. Aging heat treatment was also performed after brazing and during cooling in the same cycle.
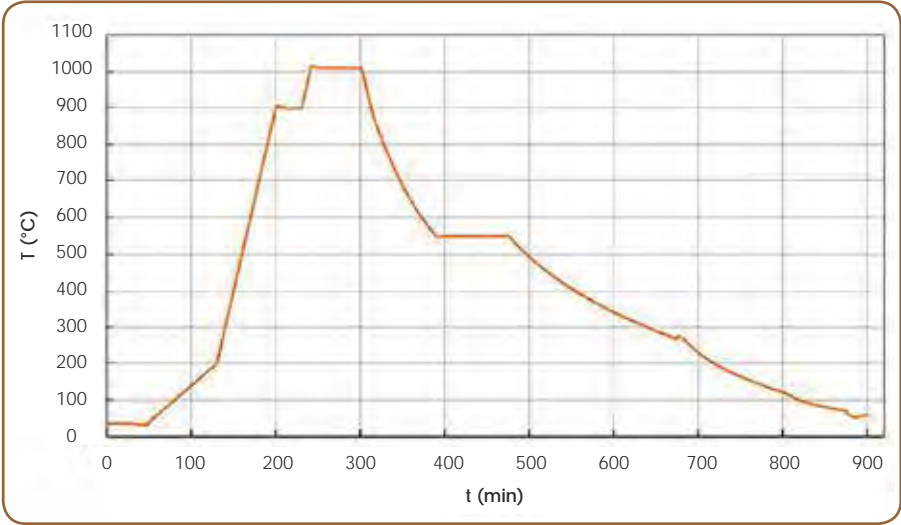

Figure 5- Brazing heat cycle

After completion of the brazing cycle, all tensile samples were machined and subjected to the tensile tests according to DIN 50125 standard. Results of these mechanical tests are summarized in Table 6, and an image of the tensile sample after failure can be seen in figure 6. The results reveal that not only the required properties of the base metal are met, but also the brazed samples are broken from the base metal area, which is an indication of higher strength of the brazed joint compared to the base metal. Furthermore, Figure 7 shows the optical microstructure of the connection area after etching. As expected, the base metal has properly maintained its tempered martensitic structure.

Figure 6- Brazed sample after tensile test

Table 6- Mechanical properties of samples

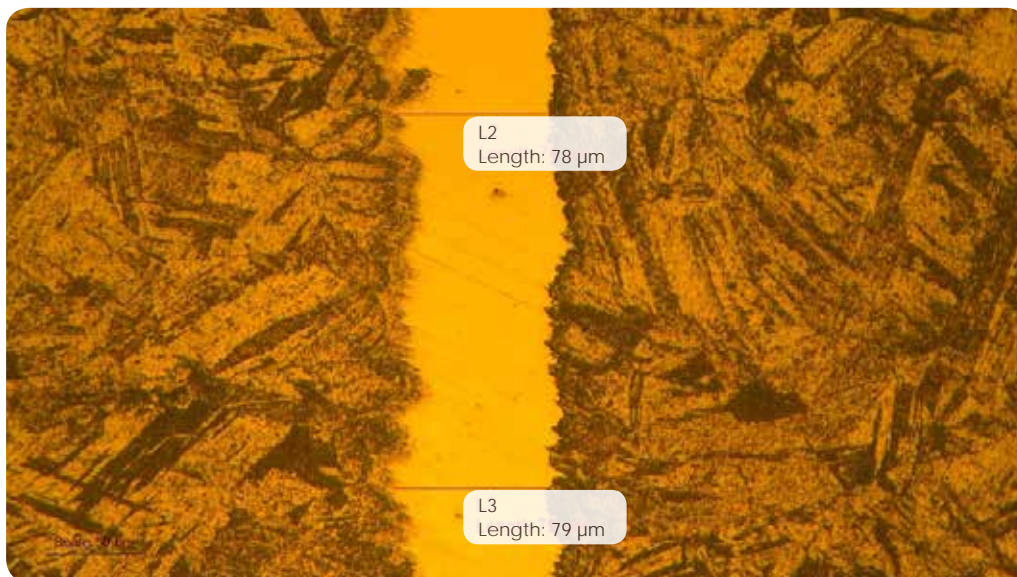|	Tensile Strength (MPa)	Yield Strength (MPa)	Elongation (%)	Hardness (HRC)	Impact Energy (J)
Brazed samples	1220	1093	18.5	-	-
Control samples	1199	1078	16	34	78

Figure 7- Microstructure of brazed sample

The scanning electron microscope image of the brazed sample is depicted in Figure 8. The results of EDS [1] analysis for the areas specified in this figure are summarized in Table 7. A eutectic structure can be observed in a region with a width of about 30 microns which complies with the chemical composition of BVAu-4 filler and the gold-nickel phase diagram (Figure 9). The

[1] Energy Dispersed Spectroscopy

analysis of area A, as a representative of this region, shows about 70% gold and 11% nickel, which justifies the formation of this eutectic structure. The analysis of area D on the brighter phase indicates a higher percentage of gold or nearness to a_1. Considering the fact that the thickness of the initial filler was 100 microns, in region B (next to the eutectic area) with a brighter background, the percentage of iron has increased, but there are still significant amounts of gold and nickel. This shows that in these regions the base metal has dissolved into the filler and a single-phase solid solution region has been formed. Furthermore, the linear analysis performed with an electron microscope (Figure 10) shows that the concentration of gold decreases with distance from the joint center and finally reaches zero in the regions of the base metal (area C). The length of the region where the gold element is observed, almost corresponds to the initial thickness of the filler, i.e. about 100 microns.
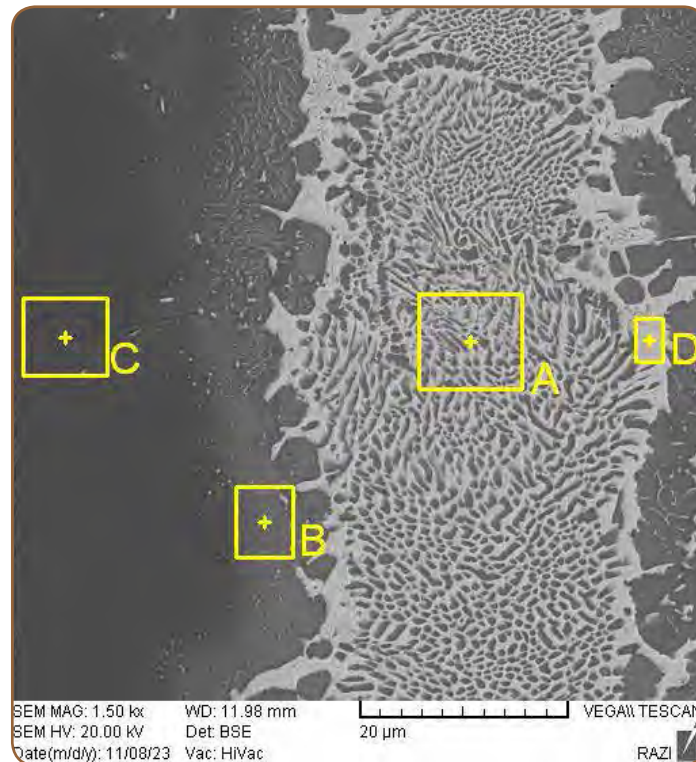

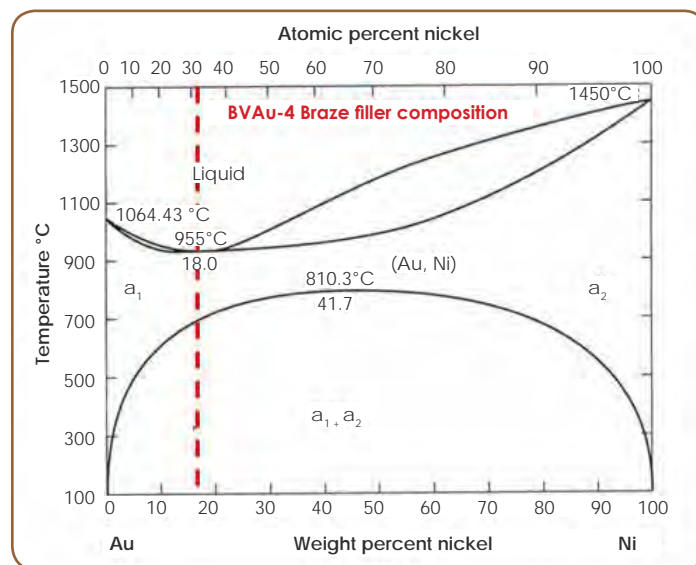Figure 8- SEM micrograph of brazed samples by BVAu-4 filler

Figure 9- Au-Ni phase diagram

Table 7- Chemical composition of EDS areas

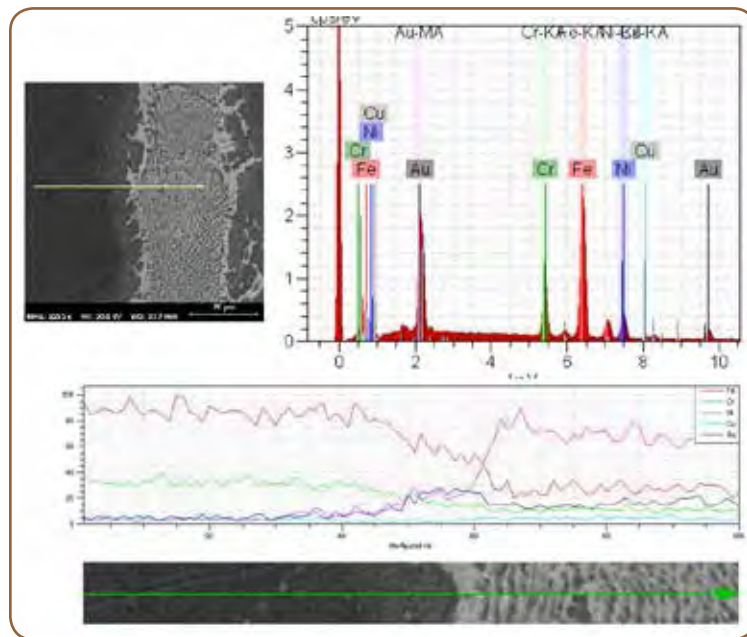| Area	%Au	%Ni	%Cr	%Cu	%Fe
A	70.94	11.14	2.30	0.8	14.76
B	10.60	28.01	9.48	1.04	50.86
C	-	4.10	15.17	3.46	75.89
D	83.12	2.03	1.57	1.61	4.09

Figure 10- EDS line scan on brazed sample by BVAu-4 filler

As the samples undergoing the brazing cycle displayed satisfactory material properties, the shear strength of the brazed joints also have to be evaluated to ensure they can be used in the highly shear-stressed operating condition of the impellers.

Evaluation of the Shear Strength of the Brazed Joints

According to the AWS C3.2M standard, samples with dimensions of 105×33×4 mm were prepared, placed in the furnace, and brazed in the previous cycle using the holding fixture shown in Figure 11 with 6 mm overlap.

Figure 11- Shear test sample in brazing fixture

After brazing, the samples were placed in the tensile test machine to be separated by shear force so that the shear strengths could be calculated via dividing the separation force by the cross-sectional area of the joint. However, as Figure 12 reveals, a distortion was observed in the joint area. This distortion means that the joint had been subjected to non-coaxial force and hence additional bending stresses. As a result, this test is inaccurate and the shear strength obtained this way will be lower than the real one.
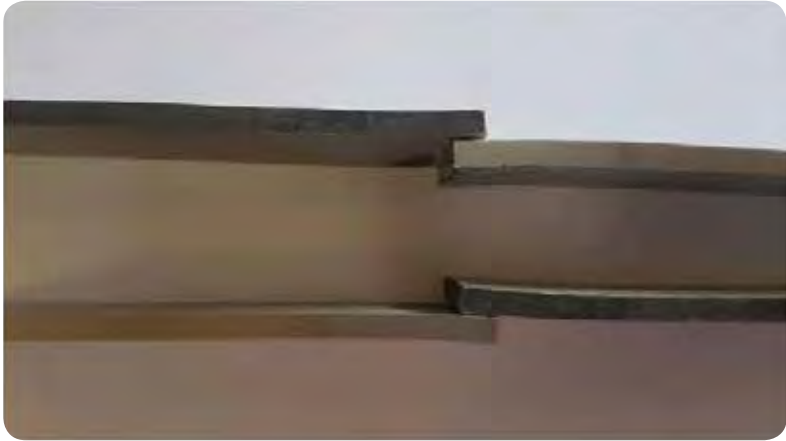

Figure 12- Shear test samples after tensile test

Eventually, it was decided to use Bulk Shear test to apply only shear force on the brazed area. In this regard, two samples were prepared and put into a fixture similar to Figure 13. The mentioned samples were subjected to compressive force under a hydraulic press so that the brazed surface would fail due to shear force. The compressive force was then divided by the brazed cross-sectional area to obtain the shear strength of the connection. As can be seen in Table 8, the shear strength of the joint area obtained from the Bulk Shear test was more than 150 MPa higher than that obtained from the previous one. This shear strength completely fulfills the mechanical design requirements of the impellers.

Figure 13- Bulk shear test sample after brazing

Table 8- Shear strength (MPa) in Bulk Shear test

Sample 1	609.59
Sample 2	621.93

Concluding Remarks

To further develop Vacuum Brazing for manufacturing impellers in MAPNA Turbine, an experiment was conducted on a gold-based, a nickel-based, and a palladium-based filler in which the gold-based filler demonstrated the highest strength in the brazed area. After further optimizing the brazing cycle, the samples were prepared and several tensile and shear strength tests were conducted to ensure that the properties of the base material (17-4PH) are maintained in this process, and the joints brazed with the gold-based filler meet the design requirements of the impellers.

The undeteriorated properties of the base metal and the desirable shear strength of more than 600 MPa at the brazed joint obtained from the test results successfully validates the effectiveness of Vacuum Brazing with the mentioned filler as a method for impeller manufacture in MAPNA Turbine.

References

[1] Shepherd, Dennis G., *"Principles of turbomachinery"* (6th ed.). New York: Macmillan. LCCN 56002849. OCLC 5899719, 1956.

[2] Japikse, David, *"Centrifugal Compressor Design and Performance"*. Concepts ETI. ISBN 978-0-933283-03-9, 1996.

[3] Scot Laney, Derrick Bauer, Akiyoshi Ando, *"Evaluation of Various Methods for Manufacturing one Piece, Small Tip Opening Centrifugal Compressor Impellers"*, ASIA Turbomachinery and Pump Symposium, Singapore, 22-25 February, 2016.

[4] S. Frier, Impeller Manufacturing – Understanding The Methods & Their Impact On Performance, 2019.

[5] M. Way, J. Willingham, R. Goodall, M. Way, J. Willingham, R. Goodall, Brazing filler metals, 6608 (2020). https://doi.org/10.1080/09506608.2019.1613311.

[6] K. Boddenberg, D. Technical, On the Manufacture 01" Impellers for Turbocompressors, 1966.

[7] J. Nowacki, Producibility of brazed high-dimension centrifugal compressor impellers, 133 174–180, 2003.

[8] ASTM A705/A705M, Standard Specification for Age-Hardening Stainless Steels Forgings, 2020.

[9] Damian Kotecki, Frank Armao, Stainless Steels Welding Guide, The Lincoln Electric Company, 2014.

[10] American Welding Society (AWS), *"A5.8 Specification for Brazing Filler Metal"*, 2019.

[11] Technical Specification, CTO 00195200-086: Palladium Braze Strips, Ekaterinburg non-ferrous metals processing plant, Organization standard, 2015.

GR656-0